



NAVAL POSTGRADUATE SCHOOL

MONTEREY, CALIFORNIA

THESIS

**OPTIMIZED GRANULARITY ANALYSIS OF
MAXIMUM POWER POINT TRACKERS IN LOW
POWER APPLICATIONS**

by

Joseph S. Madren

June 2017

Thesis Advisor:
Second Reader:

Sherif Michael
Robert Ashton

Approved for public release. Distribution is unlimited.

THIS PAGE INTENTIONALLY LEFT BLANK

REPORT DOCUMENTATION PAGE			<i>Form Approved OMB No. 0704-0188</i>	
Public reporting burden for this collection of information is estimated to average 1 hour per response, including the time for reviewing instruction, searching existing data sources, gathering and maintaining the data needed, and completing and reviewing the collection of information. Send comments regarding this burden estimate or any other aspect of this collection of information, including suggestions for reducing this burden, to Washington headquarters Services, Directorate for Information Operations and Reports, 1215 Jefferson Davis Highway, Suite 1204, Arlington, VA 22202-4302, and to the Office of Management and Budget, Paperwork Reduction Project (0704-0188) Washington, DC 20503.				
1. AGENCY USE ONLY (Leave blank)		2. REPORT DATE June 2017		3. REPORT TYPE AND DATES COVERED Master's thesis
4. TITLE AND SUBTITLE OPTIMIZED GRANULARITY ANALYSIS OF MAXIMUM POWER POINT TRACKERS IN LOW POWER APPLICATIONS			5. FUNDING NUMBERS	
6. AUTHOR(S) Joseph S. Madren				
7. PERFORMING ORGANIZATION NAME(S) AND ADDRESS(ES) Naval Postgraduate School Monterey, CA 93943-5000			8. PERFORMING ORGANIZATION REPORT NUMBER	
9. SPONSORING /MONITORING AGENCY NAME(S) AND ADDRESS(ES) N/A			10. SPONSORING / MONITORING AGENCY REPORT NUMBER	
11. SUPPLEMENTARY NOTES The views expressed in this thesis are those of the author and do not reflect the official policy or position of the Department of Defense or the U.S. Government. IRB number ____N/A____.				
12a. DISTRIBUTION / AVAILABILITY STATEMENT Approved for public release. Distribution is unlimited.			12b. DISTRIBUTION CODE	
13. ABSTRACT (maximum 200 words) Increasing energy consumption through the growing use of low-power electric devices in the U.S. military makes augmentation with solar energy an attractive solution due to its versatility, sustainability, and relatively low cost. In variable environmental conditions, solar panels generate unpredictable voltages and currents, however, which often results in power loss. Employing a maximum-power point tracker (MPPT) decouples the source and load, resulting in maximum power generation and transfer. Using Simulink, we modeled three solar array configurations and tested for the Puma AE II Small Unmanned Aerial System (SUAS) to determine optimum MPPT granularity. Distributing three MPPTs on the main wing and another on the horizontal stabilizer permitted solar panel coverage on all of the available surface area. The MPPT model tracked within 99% of theoretical power generation and transferred approximately 95% of generated power to the battery during peak environmental conditions. This configuration provided the maximum power augmentation to the SUAS battery and can extend the endurance of the Puma SUAS significantly dependent on environmental conditions, electrical load requirements, and other factors. Another conclusion is that more power can be generated with higher-efficiency cells, but the 15% Copper Indium Gallium Selenide (CIGS) cells modeled proved to be an economical approach to augmenting electrical demands on SUAS.				
14. SUBJECT TERMS MPPT, SUAS, solar efficiency, expeditionary energy, sustainable energy			15. NUMBER OF PAGES 93	
			16. PRICE CODE	
17. SECURITY CLASSIFICATION OF REPORT Unclassified	18. SECURITY CLASSIFICATION OF THIS PAGE Unclassified	19. SECURITY CLASSIFICATION OF ABSTRACT Unclassified	20. LIMITATION OF ABSTRACT UU	

THIS PAGE INTENTIONALLY LEFT BLANK

Approved for public release. Distribution is unlimited.

**OPTIMIZED GRANULARITY ANALYSIS OF MAXIMUM POWER POINT
TRACKERS IN LOW POWER APPLICATIONS**

Joseph S. Madren
Captain, United States Marine Corps
B.S., Virginia Polytechnic Institute and State University, 2004

Submitted in partial fulfillment of the
requirements for the degree of

MASTER OF SCIENCE IN ELECTRICAL ENGINEERING

from the

**NAVAL POSTGRADUATE SCHOOL
June 2017**

Approved by: Sherif Michael
 Thesis Advisor

Robert Ashton
Second Reader

R. Clark Robertson
Chair, Department of Electrical and Computer Engineering

THIS PAGE INTENTIONALLY LEFT BLANK

ABSTRACT

Increasing energy consumption through the growing use of low-power electric devices in the U.S. military makes augmentation with solar energy an attractive solution due to its versatility, sustainability, and relatively low cost. In variable environmental conditions, solar panels generate unpredictable voltages and currents, however, which often results in power loss. Employing a maximum-power point tracker (MPPT) decouples the source and load, resulting in maximum power generation and transfer. Using Simulink, we modeled three solar array configurations and tested for the Puma AE II Small Unmanned Aerial System (SUAS) to determine optimum MPPT granularity. Distributing three MPPTs on the main wing and another on the horizontal stabilizer permitted solar panel coverage on all of the available surface area. The MPPT model tracked within 99% of theoretical power generation and transferred approximately 95% of generated power to the battery during peak environmental conditions. This configuration provided the maximum power augmentation to the SUAS battery and can extend the endurance of the Puma SUAS significantly dependent on environmental conditions, electrical load requirements, and other factors. Another conclusion is that more power can be generated with higher-efficiency cells, but the 15% Copper Indium Gallium Selenide (CIGS) cells modeled proved to be an economical approach to augmenting electrical demands on SUAS.

THIS PAGE INTENTIONALLY LEFT BLANK

TABLE OF CONTENTS

I.	INTRODUCTION.....	1
A.	PROBLEM STATEMENT	1
B.	THESIS OBJECTIVES.....	2
C.	THESIS ORGANIZATION.....	3
II.	BACKGROUND	5
A.	SOLAR CELL OPERATION.....	5
1.	Photovoltaic Effect in Semiconductors	5
2.	Current-Voltage Curve of Solar Cell	8
3.	Solar Cell Parameters.....	9
4.	Solar Panel Layout.....	11
5.	Destructive Impacts of Solar Cell Mismatch.....	13
B.	MPPT	14
1.	Defining the MPP	15
2.	MPPT Algorithms.....	17
C.	POWER CONVERTERS.....	23
1.	DC-DC Converters.....	24
D.	CHAPTER SUMMARY.....	32
III.	MODELING AND EXPERIMENTAL DESIGN	33
A.	SYSTEM CONFIGURATIONS.....	33
B.	ENVIRONMENTAL CONDITIONS	37
C.	SYSTEM COMPONENTS	39
1.	Solar Cells.....	39
2.	MPPT	45
3.	Battery / Load.....	48
D.	CHAPTER SUMMARY.....	50
IV.	RESULTS	51
A.	THEORETICAL VERSUS EXPERIMENTAL POWER TRANSFER.....	51
1.	Configuration One: Four Distributed MPPT.....	51
2.	Configuration Two: Single MPPT.....	54
3.	Configuration Three: No MPPT.....	55
B.	EFFICIENCY COMPARISON.....	56
C.	CONFIGURATION COMPARISON FOR EACH TEST CASE	58
D.	CHAPTER SUMMARY.....	61

V.	CONCLUSION	63
A.	OPTIMAL GRANULARITY	63
B.	COST ANALYSIS (SYSTEM, MAINTENANCE, TACTICAL).....	64
C.	RECOMMENDATIONS FOR FUTURE WORK.....	65
1.	Test with Hardware	65
2.	Design/Build Solar Cell with MPPT Integrated Circuit	66
3.	Centralized Micro-Controller for Dynamic Logic.....	66
4.	Incorporate Telemetry Data to Better Refine Model	66
	APPENDIX.....	67
A.	CIGS SOLAR CELL SIMULATION.....	67
B.	PERTURB AND OBSERVE ALGORITHM.....	68
C.	ENVIRONMENTAL CONDITIONS SIMULATION	69
	LIST OF REFERENCES	71
	INITIAL DISTRIBUTION LIST	73

LIST OF FIGURES

Figure 1.	Atomic Structure of a Silicon Atom. Source: [6].	5
Figure 2.	Germanium Atoms Sharing Outermost Shell Electrons That Form Covalent Bonds. Source: [6].	6
Figure 3.	Photovoltaic Effect Generating an EHP. Source: [5].	7
Figure 4.	Creation of an EHP by Semiconductor Absorption of Photon. Source: [5].	7
Figure 5.	Electric Current Created by Free Electron Interaction with P-type, N-type (PN) Junction. Source: [5].	8
Figure 6.	Basic Solar Cell Model and Current-Voltage Characteristic Curve. Source: [5].	8
Figure 7.	I-V Curve and Power-Voltage (P-V) Curve Relationship. Source: [5].	10
Figure 8.	Relationship of FF and I_{SC}/V_{OC} . Source: [5].	10
Figure 9.	Series Connected Solar Cells Share Current and Add Voltage. Source: [5].	11
Figure 10.	I-V Curve of Non-shaded versus Shaded Solar Cell. Source: [5].	12
Figure 11.	Comparison of I-V Curves of Shaded and Unshaded Cells. Source: [5].	12
Figure 12.	Solar Cell Damage due to Cell Mismatch. Source: [5].	13
Figure 13.	Operation of Bypass Diode. Source: [7].	13
Figure 14.	Bypass Diodes Protecting Multiple Series-Connected Cells. Source: [8].	14
Figure 15.	Inefficient Energy Transfer of Directly Coupled DC System. Source: [10].	15
Figure 16.	Varying MPP for Different Irradiance. Adapted from [10].	15
Figure 17.	Block Diagram of Source-to-Load Decoupling. Adapted from [9].	16
Figure 18.	Feedback Loop of MPPT. Source: [11].	17

Figure 19.	Fractional Open-Circuit Values (Constant K) as a Function of Temperature and Irradiance. Source: [10].	18
Figure 20.	Topology of TEODI-Based MPPT Controller. Source: [12].	19
Figure 21.	TEODI Tracking MPP Due to Power Disparity. Source: [12].	20
Figure 22.	Perturb and Observe Algorithm. Source: [13].	21
Figure 23.	Illustration of P&O Algorithm Errors during Rapidly Changing Environmental Conditions. Adapted from [10].	23
Figure 24.	Basic Step-Down (Buck) Converter. Source: [15].	25
Figure 25.	Basic Step-Up (Boost) Converter. Source: [15].	27
Figure 26.	Basic Buck-Boost Converter. Source: [15].	28
Figure 27.	Buck-Boost Converter Modes: (a) Switch Closed and (b) Switch Open. Source [15].	28
Figure 28.	Buck-Boost Component Currents Over Time. Source: [15].	29
Figure 29.	Puma AE II Wing and Horizontal Stabilizer.	33
Figure 30.	Conceptual Layout of Four Solar Panels on Puma Wing.	34
Figure 31.	Distributed MPPT Simulink Model.	35
Figure 32.	Conceptual Layout of Two Large Solar Panels on Puma Wing.	36
Figure 33.	Single MPPT Simulink Model.	36
Figure 34.	Direct Loaded Simulink Model.	37
Figure 35.	CIGS Thin-Film PowerFlex Solar Cell by Global Solar Energy, Inc. (Product Number: FG-SM12-11).	39
Figure 36.	Dimensions for FG-SM12-11: 8.3W (6V) Solar Submodule. Source: [16].	40
Figure 37.	Manufacturer Provided I-V Curve for FG-SM12-11: 8.3W (6V) Solar Submodule. Source: [16].	42
Figure 38.	MATLAB-Generated I-V Curve of CIGS Submodule	43
Figure 39.	Simulink Model of Solar Panel	44

Figure 40.	Genasun GV-4 MPPT	45
Figure 41.	Buck-Boost Converter with MPPT Simulation	46
Figure 42.	Model of MPPT Controller Displayed in Figure 35	48
Figure 43.	Puma AE II Lithium Ion Battery. Source: [17].....	49
Figure 44.	Modified Simulink Lithium Ion Battery Model.....	49
Figure 45.	Throttle Position of Typical Raven Flight. Source: [18].	50
Figure 46.	Configuration One Individual Wing P-V Curves for Varying Environmental Conditions	51
Figure 47.	Individual Power Generated by Each Surface for 60-minute Flight of Four-Panel SUAS with Four Distributed MPPTs (Configuration One).....	52
Figure 48.	Power Transfer for 60-minute Flight of Four-Panel SUAS with Four Distributed MPPTs (Configuration One).....	53
Figure 49.	Configuration Two and Three, P-V Curves for Varying Environmental Conditions	54
Figure 50.	Power Transfer for 60-minute Flight of Two-Panel SUAS with a Single Centralized MPPT (Configuration Two).....	55
Figure 51.	Power Transfer for 60-minute Flight of Two-Panel SUAS with No MPPT (Configuration Three).....	56
Figure 52.	Comparison of Energy Transfer Efficiency between Distributed and a Single Centralized MPPT.....	57

THIS PAGE INTENTIONALLY LEFT BLANK

LIST OF TABLES

Table 1.	Product Specifications for FG-SM12-11: 8.3W (6V) Solar Submodule. Source: [16].	41
Table 2.	Configuration Performance Comparison for Test Case One	58
Table 3.	Configuration Performance Comparison for Test Case Two	59
Table 4.	Configuration Performance Comparison for Test Case Three	60

THIS PAGE INTENTIONALLY LEFT BLANK

LIST OF ACRONYMS AND ABBREVIATIONS

A	Amp
C	Capacitance
°C	degrees Celsius
CCM	Continuous Current Mode
CIGS	Copper Indium Gallium Selenide
COTS	Commercial-off-the-shelf
D	Duty Cycle
DC	Direct Current
DCM	Discontinuous Current Mode
DOD	Department of Defense
EHP	Electron-hole pair
E_{stored}	Energy stored
F	Farad
f_s	Switching frequency
FOB	Forward Operating Base
FF	Fill Factor
H	Henry
I_{SC}	Short-circuit Current
I_{MPP}	Maximum Power Point Current
I-V	Current-Voltage
K	Kelvin
L	Inductance
MPP	Maximum Power Point
MPPT	Maximum Power Point Tracking
NPS	Naval Postgraduate School
P&O	Perturb and Observe
P_{IN}	Input Power
P_{OUT}	Output Power
PN	P-type, N-type
PV	Photovoltaic

P-V	Power-Voltage
SUAS	Small Unmanned Aerial System
STC	Standard test condition
TEODI	Technique based on the Equalization of the Output operating points in correspondence of the forced Displacement of the Input
UAV	Unmanned Aerial Vehicle
V	Volt
V_{MPP}	Maximum Power Point Voltage
V_{OC}	Open-circuit Voltage
V_{OP}	Operating Voltage
W	Watt

ACKNOWLEDGMENTS

First, I must thank God for blessing me with the opportunity to further my education and the strength and focus required to complete such a formidable task. Thank you to my family, especially my wife, Rebekah, for supporting me through long nights and weekends to complete this project. Also, a special thank you to Captain Julian D’Orsaneo for helping me logistically to complete my thesis from across the country. Thank you to Dr. James Calusdian, for allowing me to invade his space and continually pester him with questions. Thank you to Major Joe O’Connor, for his priceless professional and personal mentoring. Finally, thank you to Dr. Sherif Michael and Dr. Bob Ashton, for their continued guidance, wisdom, and faith that I am capable of contributing to their field of expertise.

THIS PAGE INTENTIONALLY LEFT BLANK

I. INTRODUCTION

A. PROBLEM STATEMENT

Current technology is becoming smaller, faster, and more portable. These attributes are very attractive to the United States military, which seeks to employ systems at finer granularities to capture and disseminate data across the battlefield. One important challenge presented by portability is energy replenishment. Battery technology has advanced rapidly, allowing users to go longer and farther than ever before without having to plug into the grid; however, there are limits to the endurance of batteries. Eventually the energy must be replenished.

Consumer products are typically designed to function for a matter of hours between charges; however, military operations may last days or weeks without returning to a ship or grid-enabled location. Military units supplement the shortfall of infrastructure based electric power generation with fossil fuel electric generators. Again, these tend to be centralized and not capable of servicing the energy needs of all devices. The increasing number of devices individuals or units use that rely solely on electric power further exacerbates this problem.

Often, increasing the number of batteries, distribution of generators, etc., is not feasible. Batteries, generators, and fuel are not only expensive and heavy. The process of replenishing these critical requirements is hazardous and poses unnecessary risk to military units tasked with conducting resupply; therefore, the Department of Defense (DOD) has invested in research integrating alternative energy sources to reduce the demand for resupply. The Marine Corps created the Expeditionary Energy Office in 2009, with the mission to “deploy Marine Expeditionary Forces that can maneuver from the sea and sustain [Command, Control, Communications, Cyber, and Information] C4I and life support systems in place; the only liquid fuel needed will be for mobility systems which will be more efficient than systems are today,” by 2025 [1]. In austere locations where the noise and heat signature of traditional sources may impede mission effectiveness, alternative energy is particularly attractive.

Photovoltaic energy production (solar power) is one alternative energy source pursued by the DOD. Terrestrial based solar arrays at forward operating bases (FOBs), satellite solar arrays, and man-portable solar blankets are just some of the ways solar energy is harvested to provide electric power to the warfighter. Solar power also provides flexibility to distribute the energy production to smaller scale applications. Instead of having to charge batteries at the FOB and carry extra weight that is not being used, troops can carry a solar blanket such as SPACES II or REPPS to replenish energy “on the go” [2]. This is particularly critical as the DOD plans to network individual troops in order to gather health, ammunition, and other data using electrically powered sensors and other devices, such as the U.S. Army’s NETT Warrior Program [3].

As the primary power source available in space, solar power serves a critical function in the operation of satellites. Similarly, the DOD has extended that concept to small unmanned aerial systems (SUAS). SUAS are traditionally powered by 24–26 volt lithium ion batteries and limited to 60–120 minute flight endurance [4]. Since these systems are entirely dependent on limited battery capacity for operation, flight endurance tends to limit the mission spectrum that these systems can serve in their intelligence, surveillance, and reconnaissance roles. Augmenting the battery capacity with on-board solar energy harvesting has been a continuing research area at the Naval Postgraduate School (NPS). For this reason, in this thesis we use SUAS as a platform to conduct solar module efficiency analysis.

B. THESIS OBJECTIVES

In this project, we design a computer simulation model that can determine the optimized granularity for a maximum-power point tracking (MPPT) converter on low power solar panel arrays. Directly connecting solar panels to a battery is the least efficient method of transferring energy in a variable environment. Mobile military applications, such as a SUAS, operate in variable environmental conditions that result in unpredictable solar panel output; therefore, voltage output may drop below the threshold required to transfer power to the battery, resulting in all power generated lost as heat. Switched-mode direct-current power converters can ensure power transfer by matching

the impedance between the source and the battery; however, standard converters are typically designed to operate at fixed inputs, fixed outputs, and fixed duty cycles. Due to the varying input supplied by solar panels, a feedback mechanism must be included to adjust the duty cycle of the converter in order to ensure maximum energy harvesting from the solar panel and power conversion to satisfy battery requirements. This feedback is determined by various logic algorithms and implemented via hardware or microchip technologies. In this paper, we refer to a MPPT as a controller that includes such an algorithm. The MPPT senses the power produced by the solar panel at fixed time intervals and adjusts the duty cycle of the power converter to ensure maximum energy transfer is obtained.

MPPT technology is not new; however, it is often disregarded for low power applications for three reasons: solar panel arrays are too small to have isolated degradation due to changing irradiance, temperature, etc.; losses due to power electronics in the converter offset gains obtained by isolating the source from the load; and the cost of adding additional hardware is not worth minimal gains for non-critical consumer products. In military applications, additional gains may be required for mission critical equipment that cannot be employed in favorable environmental conditions; therefore, these reasons for not employing MPPT may be offset by mission necessity for military systems.

The concepts explored in this project are not limited to SUAS. They can be applied to any system that experiences partial or full degradation due to unavoidable varying environmental conditions. The Puma AE II SUAS was chosen due to current research at the NPS. Multiple configurations of solar arrays and converters are designed for the Puma and tested under varying environmental conditions to compare energy transfer.

C. THESIS ORGANIZATION

This paper is divided into five chapters: introduction, background, modeling and experimental design, results, and conclusion. Throughout the paper, the information is presented in an order that represents the flow of energy from the environment to the

battery. In each section, solar cells are discussed first, then MPPT, followed by power converters, then the battery and SUAS layout.

Chapter II is subdivided into three sections that review the theory incorporated in the design. In the first section, we discuss the basics of solar cell operation, metrics to evaluate the performance of solar cells, and problems associated with degradation. In the next section, a review of MPPT concepts and techniques is provided. Power conversion is discussed in the final section.

The physical systems represented by the Simulink model are presented in Chapter III. In the first section of the chapter, we introduce the solar array configurations designed for the Puma. A Copper Indium Gallium Selenide (CIGS) thin-film PowerFlex Solar Cell by Global Solar Energy, Inc. is modeled because it will be used on an actual SUAS in a future project. In the next section, the design of a MPPT implementing the perturb and observe algorithm is presented. Finally, the Simulink standard lithium ion battery is used to simulate a battery similar to that used by the Puma.

An analysis of experimental data captured from the simulation is presented in Chapter IV. In the analysis, various metrics from each configuration such as power generated, power transferred, and converter efficiency are compared. The data are also compared with expected results from theoretical calculations.

Observations of the results are presented in Chapter V. In addition, generalized costs and benefits are determined. Finally, future work related to this research area is recommended.

Throughout this paper, the term “solar cell” or “cell” refers to a homogenous photovoltaic surface. The term “submodule” refers to a number of series connected solar cells. The term “panel” refers to the arrangement of submodules and “array” refers to the arrangement of panels.

II. BACKGROUND

A. SOLAR CELL OPERATION

Photovoltaic systems (solar panels) have become increasingly attractive as a sustainable, alternative energy source over the last three decades due to fossil fuel shortages, costs, and effects on global climate change [5]. Solar power has emerged as an acceptable alternative to fossil fuels due to the decreasing cost of producing solar cells and technological advancements increasing efficiencies [5]. In this section, the basics of solar cell operation, metrics to evaluate the performance of solar cells, and problems associated with degradation are discussed.

1. Photovoltaic Effect in Semiconductors

Producing electric energy from solar irradiance is possible by the mechanism of the atomic reaction between sunlight and semiconductor material. Solar cells are “grown” as crystalline structures of periodic elements with four electrons in their outermost shell, typically silicon or germanium. The atomic structure of silicon is shown in Figure 1.

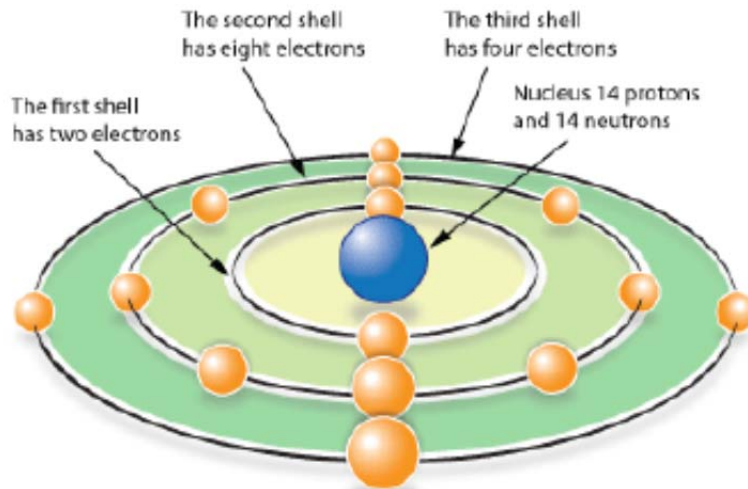


Figure 1. Atomic Structure of a Silicon Atom. Source: [6].

Adjacent atoms sharing outermost shell electrons to maintain an eight electron orbital shell form this crystal structure [6]. This phenomenon increases purity in the crystalline structure, making these materials desirable [6]. The atomic forces that hold these electrons in orbit around the nucleus are called valence bonds, and the outermost shell is referred to as the valence shell, as illustrated in Figure 2.

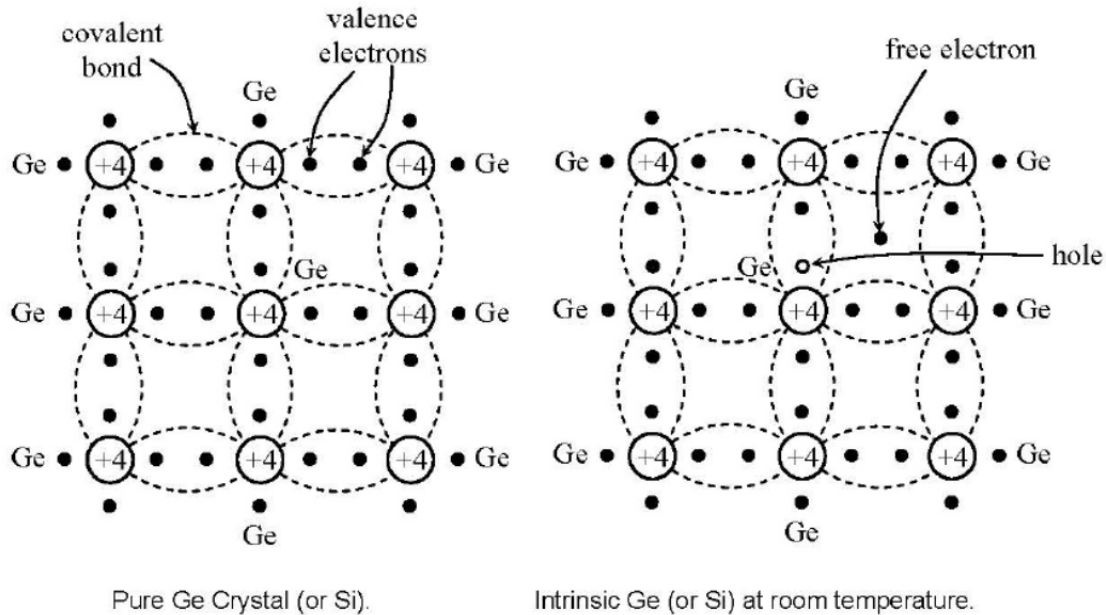


Figure 2. Germanium Atoms Sharing Outermost Shell Electrons That Form Covalent Bonds. Source: [6].

The sun emits particles of light, called photons, which contain energy. When photons maintain an energy state higher than the threshold required to break the valence bond of electrons, they are absorbed by the material. When this occurs, an electron from the valence shell breaks free and moves freely throughout the material. Conversely, the atom now missing a valence electron is positively charged. The resulting existence of a free electron and positively charged atom is referred to as an “electron-hole” pair (EHP), as shown in Figure 3.

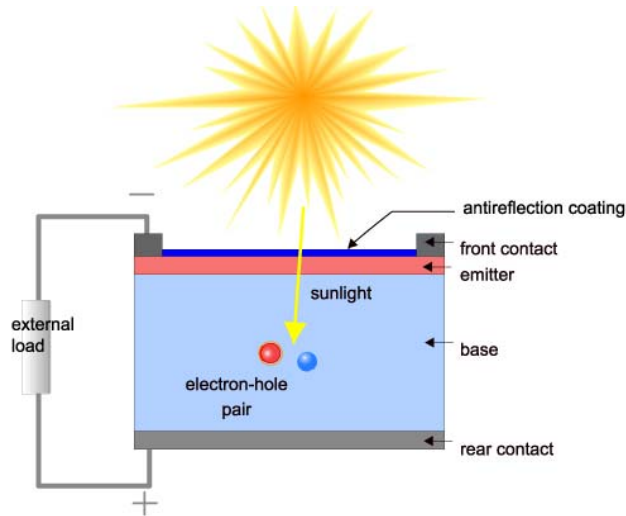


Figure 3. Photovoltaic Effect Generating an EHP. Source: [5].

The semiconductor material used to manufacture solar cells may be “doped,” intentionally introducing impurities, to increase the concentration of electrons (N-type material) or “holes,” (P-type material) [6]. Solar cells have two or more layers of differently doped material. This junction formed by the materials with different concentrations of oppositely charged atoms creates an electric field. This electric field causes the free electrons to be swept into external circuitry and recombined with a hole in the opposite material. This flow of electrons produces electric current, assuming a complete circuit exists. An illustration of this process is presented in Figures 4 and 5.

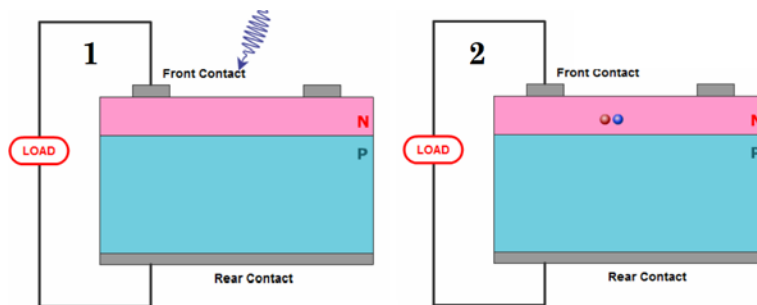


Figure 4. Creation of an EHP by Semiconductor Absorption of Photon. Source: [5].

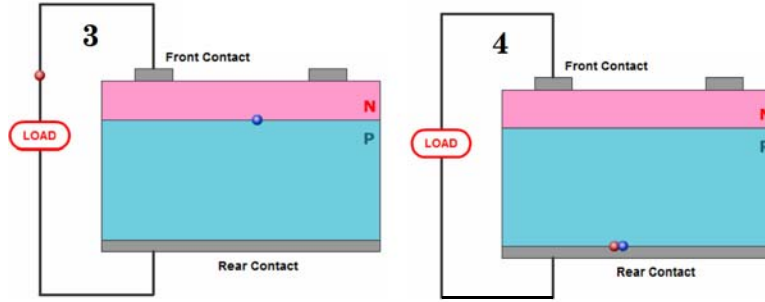


Figure 5. Electric Current Created by Free Electron Interaction with P-type, N-type (PN) Junction. Source: [5].

The free electron may recombine with a hole before it is swept into the circuit by the electric field. Similarly, there are also instances where photons either do not have requisite energy to break valence bonds or simply do not strike atoms. In each case, the energy of the irradiated photon is not harvested, reducing efficiency. Much research on solar cell design is devoted to countering these inefficiencies, which is beyond the scope of this paper.

2. Current-Voltage Curve of Solar Cell

A solar cell can be modeled as a current source and a diode (excluding series and shunt resistance of the solar cell). This model and associated current-voltage curve (I-V curve) are presented in Figure 6.

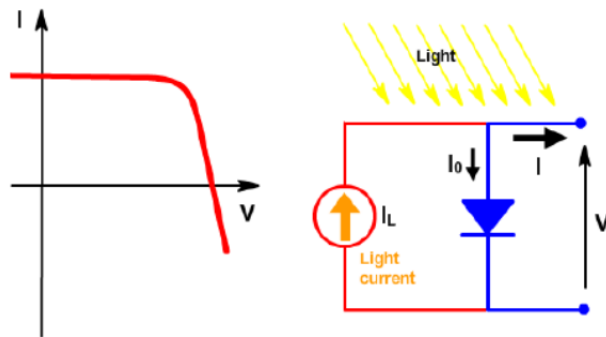


Figure 6. Basic Solar Cell Model and Current-Voltage Characteristic Curve. Source: [5].

This curve is similar to that of a PN-junction diode; however, since the semiconductor is producing energy, the curve has been rotated in the first quadrant. The current generated by the solar cell I_{total} is calculated as

$$I_{total} = I_{ph} - I_o \left[e^{qV/nkT} - 1 \right], \quad (1)$$

where

I_{total} = the net current flowing through the circuit;

I_{ph} = the current generated in the cell by incident light;

I_o = the diode leakage current in the absence of light;

V = the voltage applied across the PN junction;

q = absolute value of electron charge;

k = Boltzmann's constant;

n = quality factor based on material characteristics; and

T = temperature (K).

3. Solar Cell Parameters

The short-circuit current I_{SC} and open-circuit voltage V_{OC} are parameters used to measure the performance of a solar cell. These two values define the boundary of the current-voltage (I-V) curve as the maximum possible current and voltage, respectively. The solar cell operates at a current and voltage value less than these maximums.

Power is zero at the maximum current or voltage, as shown in Figure 7. Since power equals current multiplied by voltage, the maximum of the power curve identifies the current and voltage that produce the maximum power, referred to as I_{MPP} and V_{MPP} , respectively. The fill factor FF of a solar cell is the ratio of the maximum power of a solar cell to the product of I_{SC} and V_{OC} ,

$$FF = \frac{I_{MPP} V_{MPP}}{I_{SC} V_{OC}} \times 100\%. \quad (2)$$

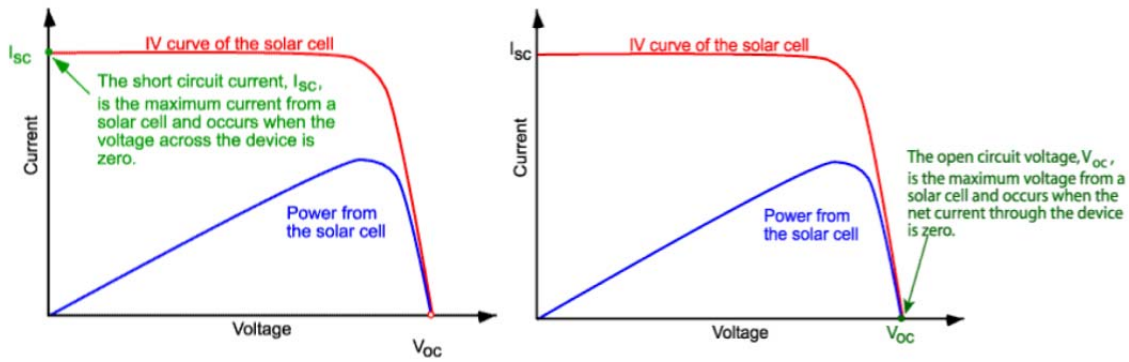


Figure 7. I-V Curve and Power-Voltage (P-V) Curve Relationship. Source: [5].

As illustrated in Figure 8, the maximum power point (MPP) occurs at V_{MPP} and I_{MPP} and is a function of FF . Monocrystalline silicon solar cells typically exhibit FF s ranging from 75–85% [5].

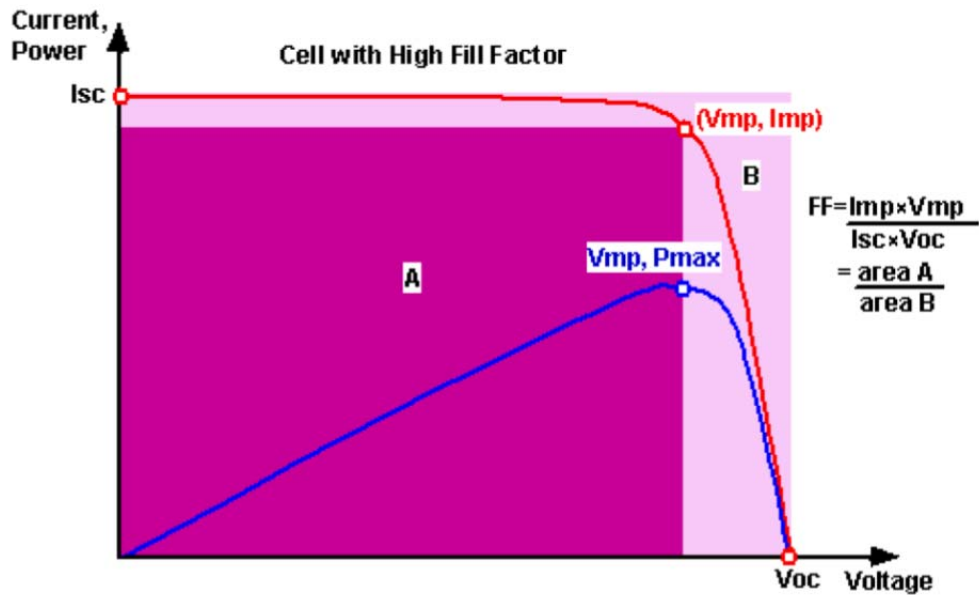


Figure 8. Relationship of FF and I_{sc}/V_{oc} . Source: [5].

Fill factor should not be confused with efficiency. Efficiency is a measure of the output power P_{out} of a solar cell with respect to the input power P_{in} contained within the

photons exposed to a cell. Efficiency η is the primary parameter used to compare multiple cells under precise conditions defined by industry standards. Efficiency is calculated

$$\eta = \frac{P_{out}}{P_{in}} = \frac{I_{sc} V_{oc} FF}{P_{in}}. \quad (3)$$

4. Solar Panel Layout

The generated V_{oc} of a single silicon solar cell is typically between 0.5-0.7 V due to physical constraints [5]. Because this operating voltage is below the threshold to charge most commercial grade batteries or to tie into an electrical grid, solar cells are connected in series to increase the overall voltage of the system. For instance, a panel may contain 60 series-connected silicon cells, each capable of generating 0.6 V at V_{oc} , for a total panel output rating of 36.0 V. Recall that series connected elements in an electric circuit must have the same current. The additive effect on voltage of solar cells connected in series is illustrated in Figure 9.

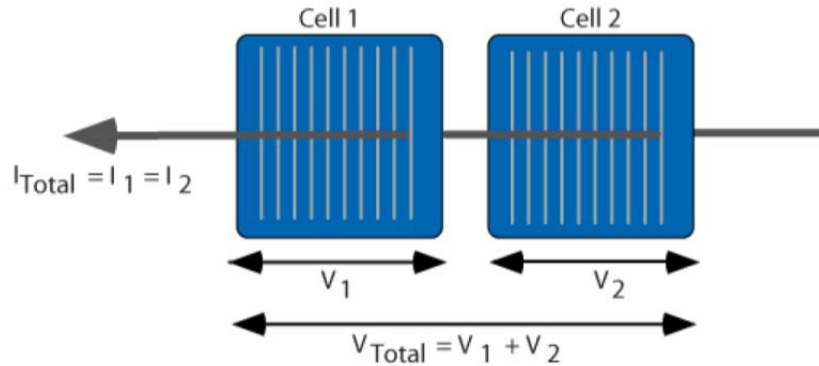


Figure 9. Series Connected Solar Cells Share Current and Add Voltage. Source: [5].

If a solar cell experiences a lower irradiance (due to shading, obscuration, etc.), it produces a lower current, as illustrated by Figure 10; therefore, the higher current generated in cells experiencing higher irradiance must be metered to meet the constraints of the least producing cell. A comparison of shaded versus unshaded solar cells connected in series is presented in Figure 11. The excess power associated with the

higher current is released in the form of heat. The dissipation of this heat can be destructive in lower power producing solar cells.

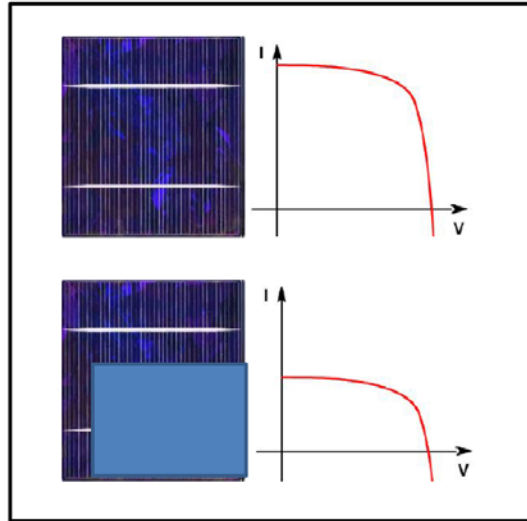


Figure 10. I-V Curve of Non-shaded versus Shaded Solar Cell. Source: [5].

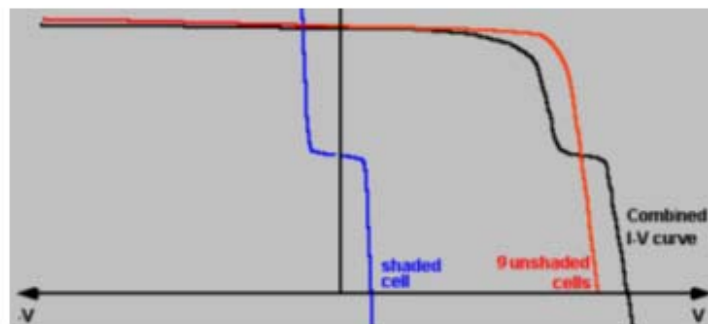
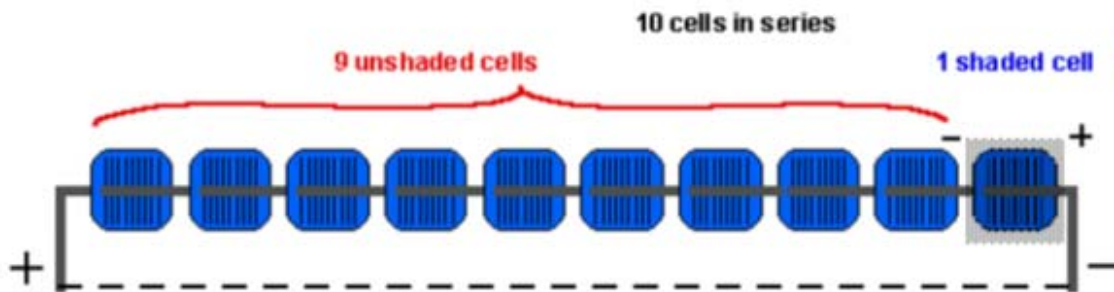


Figure 11. Comparison of I-V Curves of Shaded and Unshaded Cells. Source: [5].

5. Destructive Impacts of Solar Cell Mismatch

Solar cell “mismatch” is the dissipation of heat in solar cells due to varying energy production of series connected cells and presents a serious problem for equipment lifespan [5]. If not dissipated appropriately, the heat generated by excess energy can destroy solar cells and seriously degrade the performance of panels, as seen in Figure 12.



Figure 12. Solar Cell Damage due to Cell Mismatch. Source: [5].

One solution to solar cell mismatch is to implement a bypass diode. In normal conditions, the bypass diode remains reverse biased and does not conduct electric current; however, in the case that one cell or group of cells begins to perform poorly, the diode forward biases and conducts current, bypassing the poor performing cell, as displayed in Figure 13.

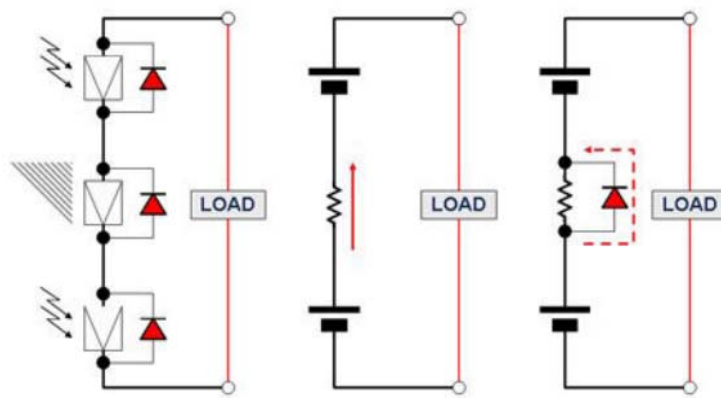


Figure 13. Operation of Bypass Diode. Source: [7].

The bypass diode ensures maximum current flow through the panel and protects the equipment. Typical configurations consist of one bypass diode for multiple series connected cells, as seen in Figure 14. The breakdown voltage of a single poor-performing cell determines the number of cells that can be protected by a single diode.

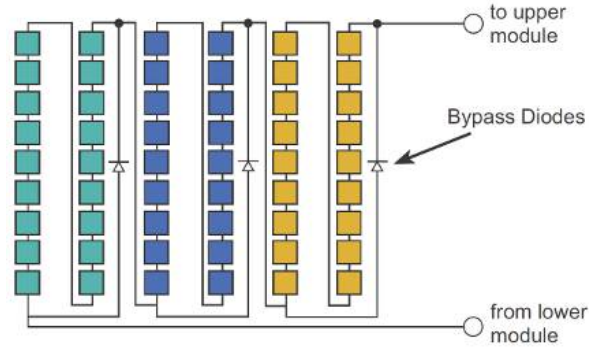


Figure 14. Bypass Diodes Protecting Multiple Series-Connected Cells. Source: [8].

B. MPPT

Since the invention of solar panels, people have been exploring methods to maximize efficiency. Much of this research has focused on the materials and construction of the actual solar cell. Some has focused on maximizing efficiency from a system of solar panels, such as maximizing the system power by matching the impedance of the solar panel (source) with the battery or grid (load) to create a Thevenin equivalent circuit. This is the process of MPPT, which uses external circuitry to adjust voltage and/or current parameters to achieve impedance matching. Over 19 different techniques or algorithms have been developed, each with advantages and disadvantages depending on the application [9]. In this section, we present the theoretical concepts of MPPT and review three popular techniques to provide exposure to the spectrum of methods: the fractional open-circuit voltage method; the “Technique based on the Equalization of the Output operating points in correspondence of the forced Displacement of the Input operating points (TEODI) [10]; and the perturb and observe (P&O) method of MPPT.

1. Defining the MPP

Maximum power from a source is transferred to a load when the characteristic impedance of both match. When DC sources are directly coupled to loads, the impedances rarely match, causing some energy generated to be lost as heat, as displayed in Figure 15.

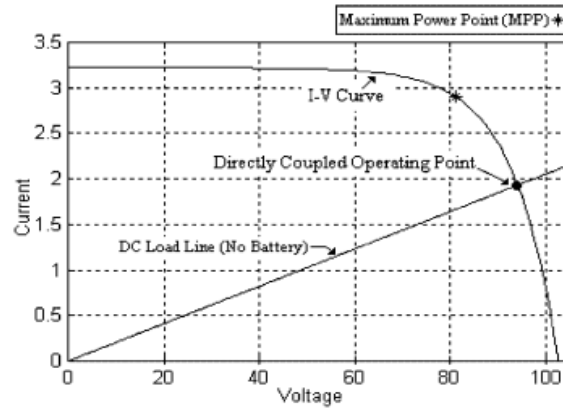


Figure 15. Inefficient Energy Transfer of Directly Coupled DC System.
Source: [10].

Further compounding this situation, the impedance of photovoltaic sources is constantly changing due to varying irradiance, temperature, and other factors, as seen in Figure 16.

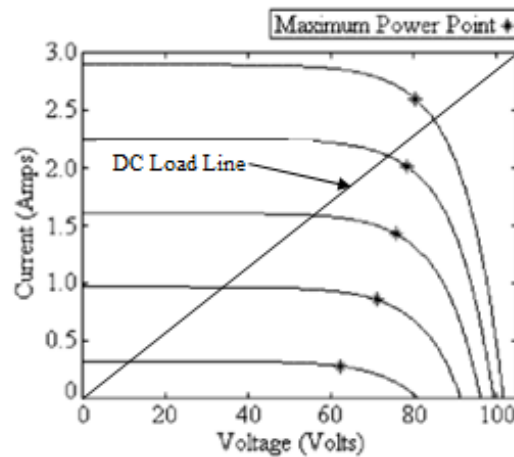


Figure 16. Varying MPP for Different Irradiance. Adapted from [10].

With a relatively static impedance load, such as a battery, only a fraction of the energy generated by the source is transferred.

Directly coupling the source to the load is the preferred method of transferring energy because it minimizes components and failure points; however, directly coupled systems result in significant power transfer losses in variable environments. MPPT maximizes power transfer by decoupling the load from the source. Typically, the additional circuitry is a power converter capable of tracking the MPP. This converter is placed between the source and the load and adjusts parameters, such as voltage and/or current, as represented in the block diagram in Figure 17.

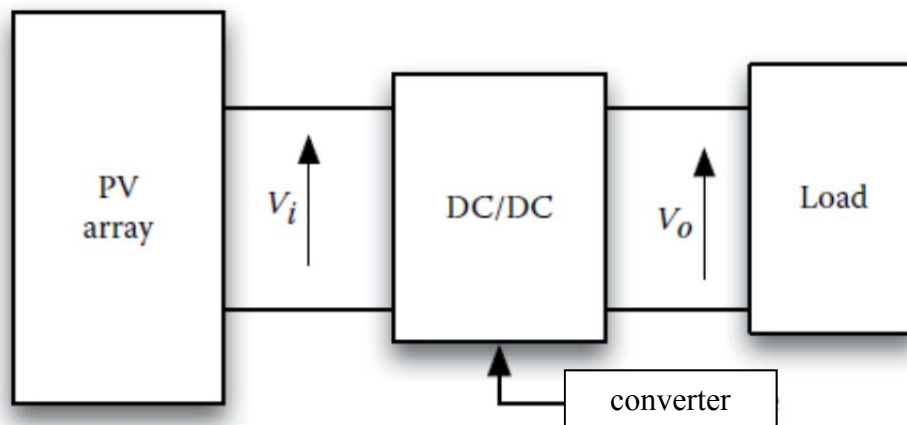


Figure 17. Block Diagram of Source-to-Load Decoupling.
Adapted from [9].

Placing a converter between the source and the load creates power losses associated with converter operation. Often referred to as insertion losses, the power consumed by the converter components must be low enough to justify a net system gain. Small-scale photovoltaic applications typically employ switching converters due to their small size and high efficiencies. The feedback mechanism used by the MPPT controller to adjust the switching frequency, or duty cycle, of a DC-DC power converter is illustrated in Figure 18.

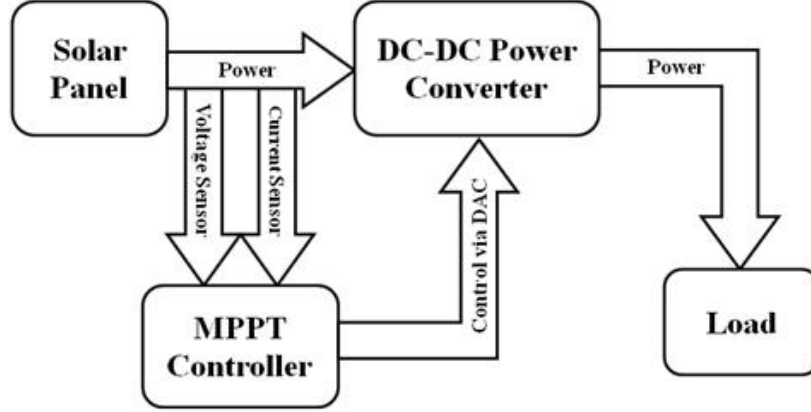


Figure 18. Feedback Loop of MPPT. Source: [11].

2. MPPT Algorithms

In general, there are two types of MPPT techniques, indirect and direct. Indirect techniques typically have preset operating points and are most effective with homogenous arrays operating under predictable conditions (i.e., solar farm in a desert environment). Direct techniques take a more active approach, measuring source parameters and adjusting converter operation through feedback mechanisms. These techniques are better suited for situations in which irradiance is variable (i.e., potentially cloudy areas). Each technique has advantages and disadvantages; thus, the net benefit of employing a technique depends on the application.

a. Fractional Open-Circuit Voltage

Fractional open-circuit voltage is an indirect method that works well with a system that experiences similar temperatures and little irradiance disruption. This technique takes note of the fact that V_{MPP} is always less than V_{OC} . Furthermore, V_{OC} remains relatively constant for a wide range of irradiance and temperature values; therefore, the literature suggests V_{MPP} is predictability between 0.74 and 0.82 that of V_{OC} , as depicted in Figure 19 [10].

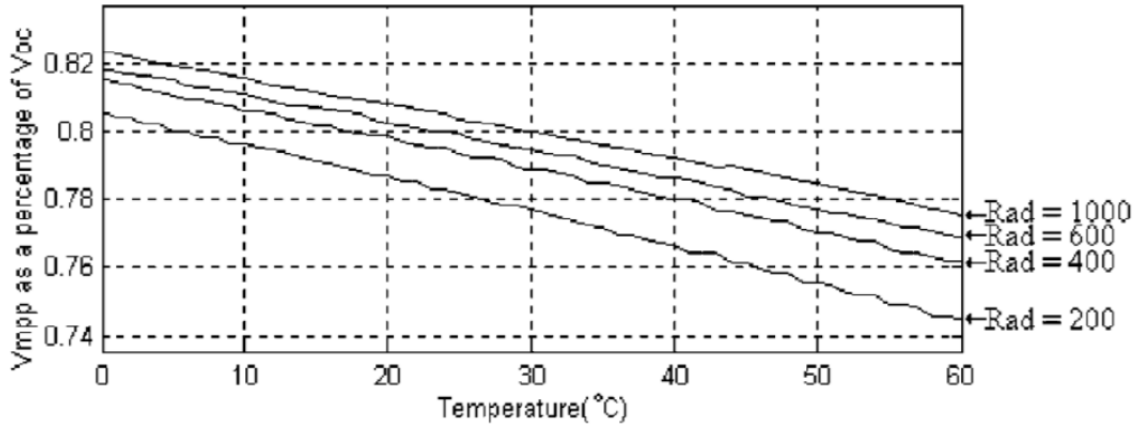


Figure 19. Fractional Open-Circuit Values (Constant K) as a Function of Temperature and Irradiance. Source: [10].

The ratio of V_{MPP} and V_{OC} can be represented by a constant K ,

$$\frac{V_{MPP}}{V_{OC}} = K \rightarrow (K \leq 1). \quad (4)$$

This method can provide slightly more dynamic tracking of the MPP by periodically sampling the open-circuit voltage. Even if power output is diminished due to a varying irradiance, the output power is close to the maximum power transfer due to operating at the adjusted voltage point. The monitoring of the open-circuit voltage is accomplished in one of two ways: 1) momentarily disconnecting the circuit to measure the open-circuit voltage; or 2) using a small, independent solar cell of similar composition to a larger panel or array, called a “pilot cell.” The advantage of using a pilot cell is that power transfer of the circuit is not disrupted; however, the pilot cells electrical characteristics must be identical to the remainder of the panel for true representation. This can be complicated in larger arrays, where the silicon used in various panels may not be of the same manufacturing batch. Furthermore, if a panel were to fail or be damaged, its replacement is almost guaranteed to be different from the pilot cell. Conversely, opening the circuit to measure the parameters disrupts power transfer, which results in losses.

b. *TEODI*

An indirect approach, TEODI, equalizes the output parameters of two identical photovoltaic systems in order to track the MPP [10]. Topologies that employ TEODI assign individual converters to subsections connected in parallel and share a common controller, as depicted in Figure 20.

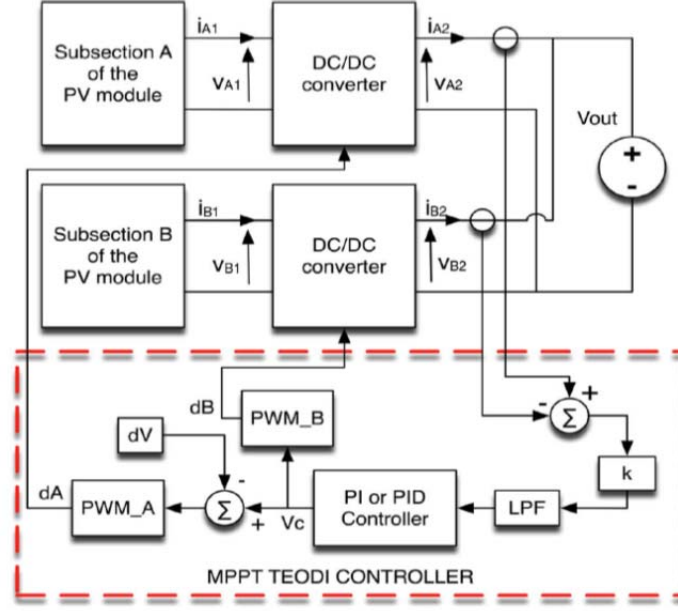


Figure 20. Topology of TEODI-Based MPPT Controller.
Source: [12].

Since the converters are connected in parallel, the output voltages are equal. Differences in output currents result in different power outputs, which represent a disparity in the operating point. Since the voltage-power curve is only flat at the MPP, any difference in output current means the system is not operating at the MPP.

Subsection (A) in Figure 20 is represented by a square in Figure 21, and subsection (B) is represented by a circle. From Figure 21(a), subsection (A) clearly produces more power than subsection (B); however, the parallel configuration of converters ensures that they are producing the same output voltage. In this case, the controller correlates the difference in power with a difference in output current of the

converters, $i_A > i_B$. Similarly, the opposite situation on the other side of the MPP is illustrated in Figure 21(b); thus, the controller sends a signal corresponding to $k(i_A - i_B)$ to the DC-DC controllers in order to adjust the duty cycle to match the output currents. Once matched, the output power sensed by the controller is equal, as represented in Figure 21(c).

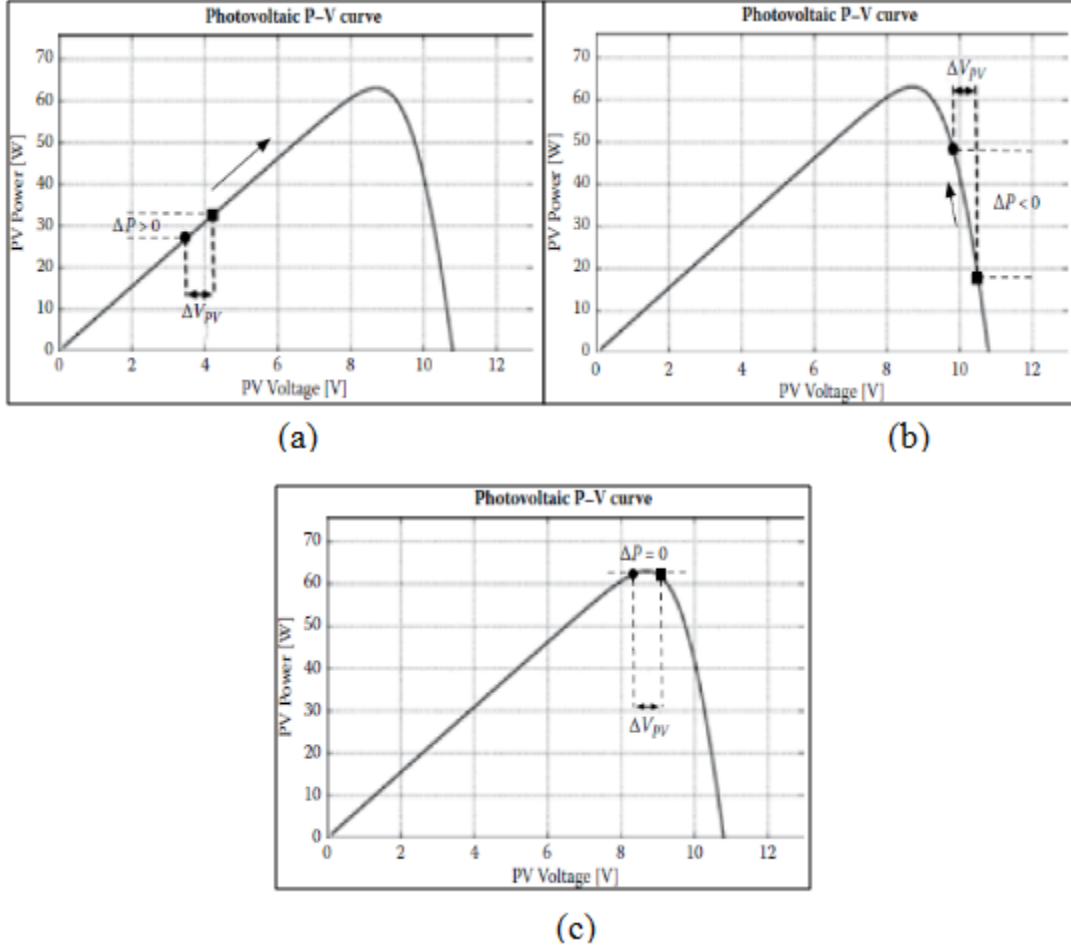


Figure 21. TEODI Tracking MPP Due to Power Disparity.
Source: [12].

The advantages of this TEODI include linear methods as opposed to switching methods, less sensitivity to varying environmental conditions, and no oscillation around MPP in real conditions. The primary disadvantage is that it requires both PV systems to be characteristically identical, which is rare; however, TEODI is suitable for small-scale

applications where the submodules of a panel or subpanel were manufactured together and are uniform.

c. *Perturb and Observe*

The most popular of all MPPT algorithms is a direct approach called perturb and observe (P&O). Similar to fractional open-circuit voltage, P&O measures the parameters of the source and makes adjustments to track the MPP; however, two main differences exist between P&O and fractional open-circuit voltage: 1) P&O uses a feedback loop to actively track the results of parameter adjustment; 2) P&O uses active components (i.e., voltage controlled switch) to control the output parameters presented to the load. The logical design of P&O is presented in a flowchart in Figure 22.

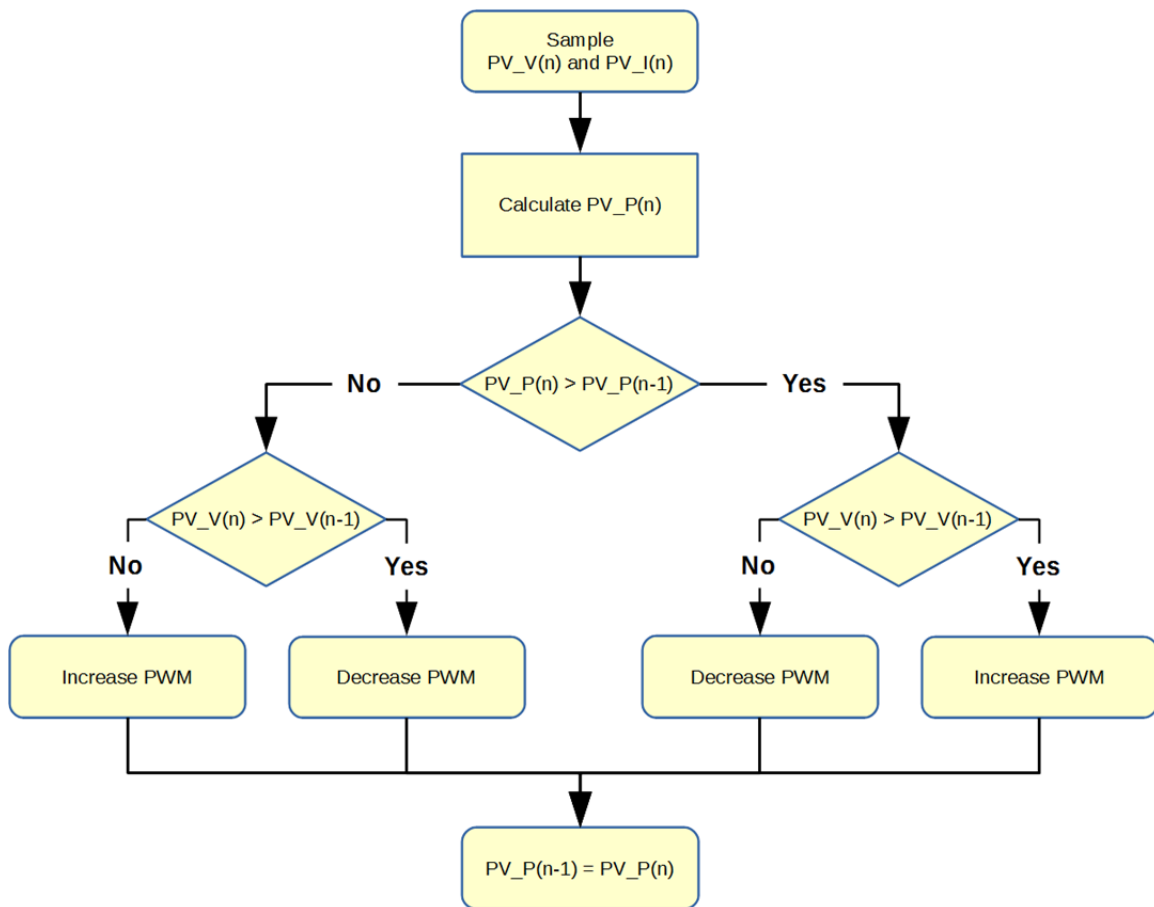


Figure 22. Perturb and Observe Algorithm. Source: [13].

As the MPPT components measure output voltage, current, or both from the photovoltaic source, a small perturbation is introduced by adjusting the duty cycle of a DC-DC converter to reduce (buck) or increase (boost) the output voltage. Power parameters are measured again to determine if the algorithm is tracking in the correct direction. This continuous process ensures the system operates near the MPP for varying environmental conditions.

Although P&O is an effective algorithm, especially during varying environmental conditions, drawbacks exist. In Figure 23, four sampling periods of the P&O controller are represented by t_1 - t_4 . In the first period, the power sensed is less than the MPP and the operating voltage $V_{OP} < V_{MPP}$, so the MPPT adjusts the voltage to a larger value. At the next sample, the power is still less than the MPP but $V_{OP} > V_{MPP}$, so the MPPT decreases the voltage; however, rapidly changing environmental conditions generate a new larger MPP, as represented by curve two. As a result, the MPPT senses a larger power generated during the next sample. Although the sensed power output is less than the new MPP, the MPPT logic deduces tracking in the correct direction. It is clear that the effect of rapidly increasing irradiance on power computation causes the MPPT to track further away from the MPP. Subsequent adjustments required to get back to MPP can result in significant insertion losses.

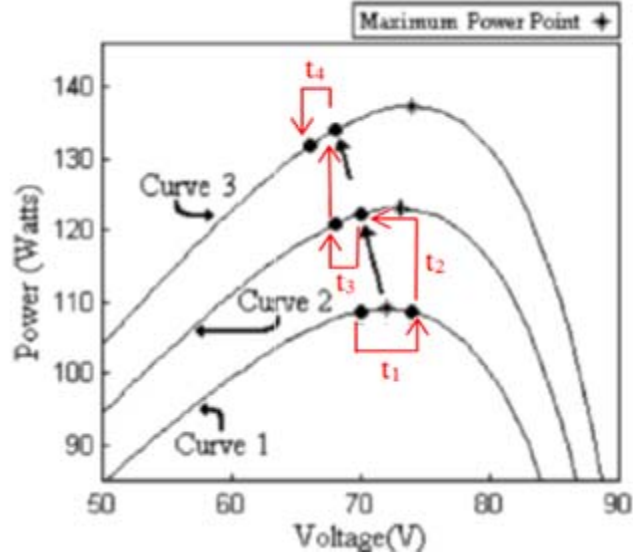


Figure 23. Illustration of P&O Algorithm Errors during Rapidly Changing Environmental Conditions. Adapted from [10].

The main disadvantage of P&O is that it requires active components that introduce insertion losses. Another disadvantage is that incremental step size tends to be fixed and can introduce errors. If the step size is too large, the control algorithm may oscillate around the MPP, introducing unnecessary insertion losses. Finally, the system may lag behind changing variables if step size is too small. This is further compounded by rapidly changing variables that cause the system to track in the opposite direction and can result in significant power losses. In other words, dynamic response may conflict with the controller operation.

Despite drawbacks with P&O in extreme cases, it is very popular and widely used in commercial-off-the-shelf (COTS) MPPT capable power converters. Some manufacturers modify this algorithm slightly for increased efficiency, often as proprietary logic in microchips. Due to its wide proliferation in COTS products and simplicity for implementation, P&O is the algorithm used in this research.

C. POWER CONVERTERS

Power processing systems are instrumental to most energy transfer systems. By processing power through one or multiple stages, we can adjust parameters such as

voltage, current, or both to comply with component ratings of the source or load; therefore, each stage, referred to as a power converter, is the basic building block upon which power processing occurs to permit different types of power electronic subsystems to operate within a single system [14].

Power conversion processes may be divided into two categories: linear and switching electronics. Linear electronics refers to circuits that operate semiconductor devices in their linear (active) region. These applications are typically less expensive, heavier, and less efficient than switching electronics [14]. Switching electronics refers to circuits in which transistors are operated as switches (either fully on or off). When the semiconductor device is used as a switch, the circuit can operate at much higher efficiencies. The semiconductors are not used as resistors, avoiding typical loss associated with linear circuits.

In this research, we focus on military systems with limited power generation capacity. Due to their high efficiency, switching converters are more suited for these applications, and in this project, we focus on solar generated DC power transfer to a DC battery. In this section we focus only on power-electronic DC-DC converters.

1. DC-DC Converters

A DC-DC converter, sometimes referred to as a voltage regulator, is most commonly used to convert an unregulated DC voltage input into a controlled constant magnitude DC voltage output. Due to irradiance and temperature fluctuations, photovoltaic sources produce fluctuating voltage. As such, a DC-DC converter may be used to level fluctuating voltage for a constant voltage load. In this section, we discuss the operation of the three types of direct coupled DC-DC converters: Buck, Boost, and Buck-Boost.

As covered in Chapter 7 in [14], all three converters share the most basic components. Each converter has a source, a switch, a diode, an inductor, a capacitor, and a load. Each converter also uses the energy storage characteristics of the inductor and capacitor to balance how much energy is transferred to the load. Finally, all three converters can operate in one of two basic modes: continuous-conduction mode (CCM)

or discontinuous-conduction mode (DCM). Since each mode gives the circuit significantly different characteristics, it is important to design a converter and control mechanism based on both modes of operation or to size components appropriately to ensure a predictable mode of operation [14].

In this research, we employ a direct coupled buck-boost converter since the solar array applied to the SUAS consists of differently sized solar panels that can produce voltages above or below the fixed operating voltage of the battery, depending on environmental conditions. Furthermore, the converter is designed to operate in a mode that maintains a minimum current above zero, called CCM. This mode simplifies the control of the duty cycle input and results in a predictable closed form output; therefore, while the operation of buck and boost converters is discussed briefly, the most detailed explanation is provided for a buck-boost converter since the other two converters operate by similar mechanisms. As a note, the buck-boost converter is an amalgamation of a buck converter and a boost converter.

a. Buck Converters

A step-down DC-DC converter, referred to as a buck chopper or buck converter, reduces the output voltage to some fraction of the input voltage. The basic buck chopper circuit is presented in Figure 24.

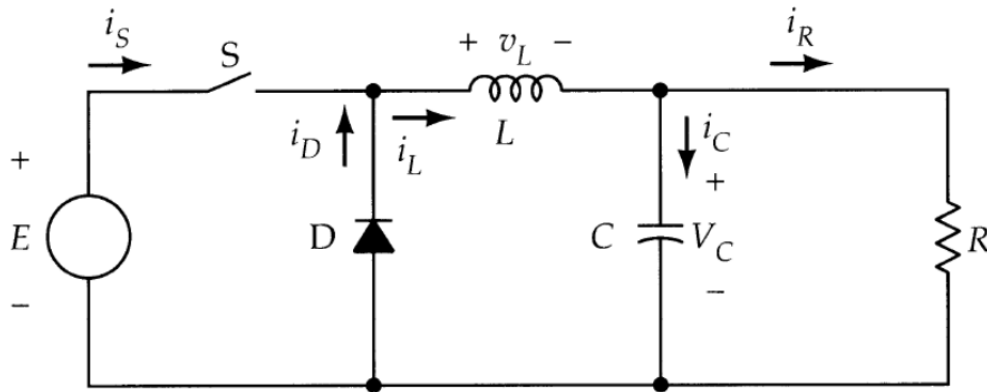


Figure 24. Basic Step-Down (Buck) Converter. Source: [15].

The operation of a buck chopper is based on storing magnetic energy in the passive elements. When the switch is closed, the inductor begins storing energy in the form of rising electric current, $E_{stored} = \frac{1}{2}LI^2$, where E_{stored} is the magnetic energy stored, L is the inductance, and I is the electric current. Likewise, the capacitor builds charge and stores electrostatic energy in the form of voltage, $E_{stored} = \frac{1}{2}CV^2$, where C is the capacitance, and V is the voltage. Since the capacitor is generally large, the time-varying voltage across the capacitor can be represented by a DC value, $v_c(t) = V_C$. Also, since the capacitor is in parallel with the load, the output voltage is referred to as V_C .

When the switch is opened, the source is electrically isolated from the circuit, and the inductor and capacitor begin to discharge their energy into the load. The switching operation takes place many times per second, called the switching frequency f_s . The amount of time the switch is closed for a given period, $T = 1/f_s$, is called the duty cycle D . Assuming the inductor is large enough to ensure CCM, we calculate the output voltage as a fraction of the input voltage E weighted by the duty cycle, $V_C = DE$, using Kirchhoff's voltage law [14]; therefore, the maximum output voltage is equal to the input voltage ($D = 1$). The optimal duty cycle range, $0.5 \leq D \leq 0.9$, ensures the converter provides output voltages between 50% and 90% of input voltages, respectively.

b. Boost Converters

The operation of the step-up (boost) converter is the exact opposite of the buck converter. The boost converter produces an output voltage that is larger than the input voltage [14]. As depicted in Figure 25, the inductor in a boost converter is on the source side of the switch.

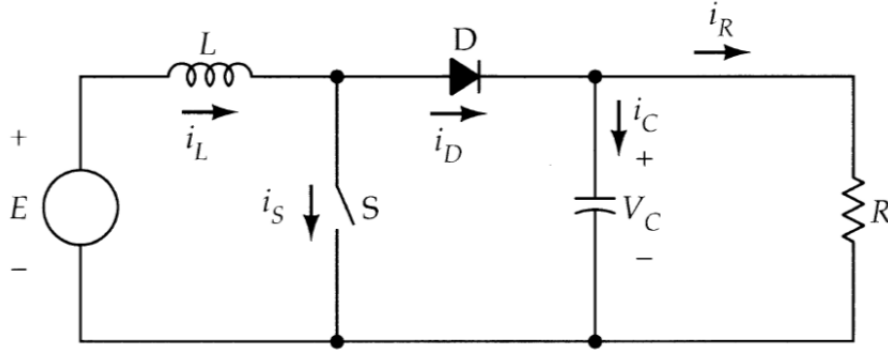


Figure 25. Basic Step-Up (Boost) Converter. Source: [15].

When the switch is closed, the source is electrically isolated from the load because all current flows through the short resulting from the closed switch. In this case, energy is transferred to the inductor in the form of electric current. When the switch is open, the load receives energy from the source and the inductor; therefore, the voltage across the load of a boost converter is always greater than the source voltage. Using Kirchhoff's voltage law, we can compute the voltage across the load as

$$V_C = \frac{E}{(1-D)} . \quad (5)$$

The more the switch is closed, the more output voltage gain can be realized. This must be balanced with physical limitations to ensure components do not fail or the system become uncontrollable; therefore, the duty cycle range of $0 \leq D \leq 0.5$ is recommended. This ensures the circuit performs safely while accomplishing gains between 1.11 to 2.00 times that of input voltages.

c. **Buck-Boost Converters**

The last converter to be reviewed is the combination of the buck chopper and the boost converter, which is appropriately referred to as the buck-boost converter. Buck-boost converters can either step-up or step-down voltage depending on duty cycle [14]. An image of a buck-boost converter is presented in Figure 26.

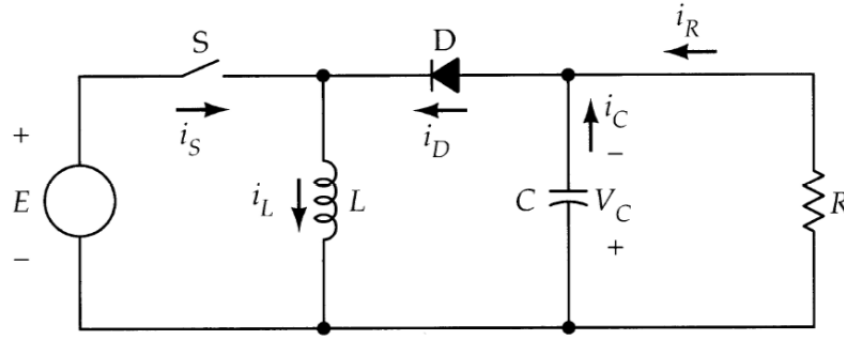


Figure 26. Basic Buck-Boost Converter. Source: [15].

The components of the buck-boost converter mirror those found in the two previously mentioned converters, just arranged differently. Furthermore, just as before, the inductor is the critical energy storage device for operation of the buck-boost converter. Switch open or switch closed, the source is effectively electrically isolated from the load because the diode is reverse biased, as depicted in Figure 27. When the switch is closed, the source transfers energy to the inductor, as depicted in Figure 27a. When the switch opens, the inductor discharges that energy to the load via the negative terminal, as depicted in Figure 27b. Significantly, during the operation of this converter, the polarity of the output voltage is inverted with regard to convention; therefore, to ensure positive voltage at the output, the connection to the load needs to be reversed.

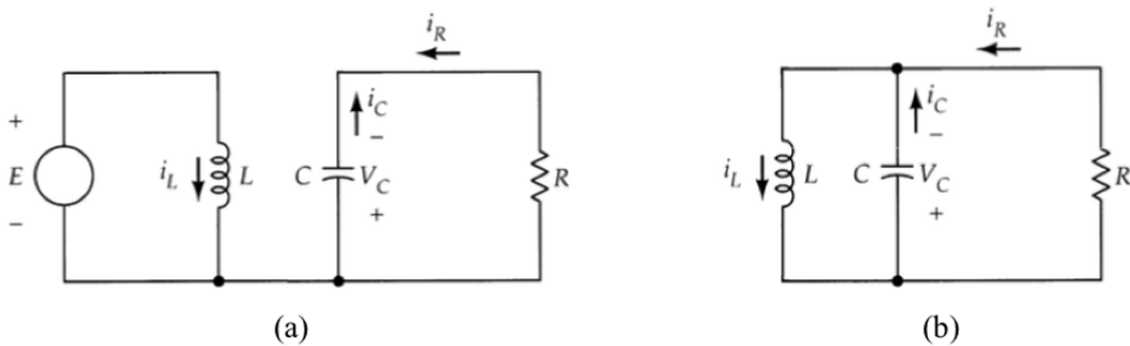


Figure 27. Buck-Boost Converter Modes: (a) Switch Closed and (b) Switch Open. Source [15].

In computing the relationship of input and output voltages, it becomes even more apparent that the buck-boost converter operates like a combination of the two previously mentioned converters. When the switch is closed, as shown in Figure 27a, the circuit operates just like a boost chopper with the switch closed. Using Kirchhoff's voltage law,

$$E = v_L = L \frac{di_L}{dt}, \quad (6)$$

and by rearranging and integrating, we get

$$I_{\max} - I_{\min} = \frac{E}{L} DT. \quad (7)$$

The circuit currents computed in (7) are depicted graphically in Figure 28.

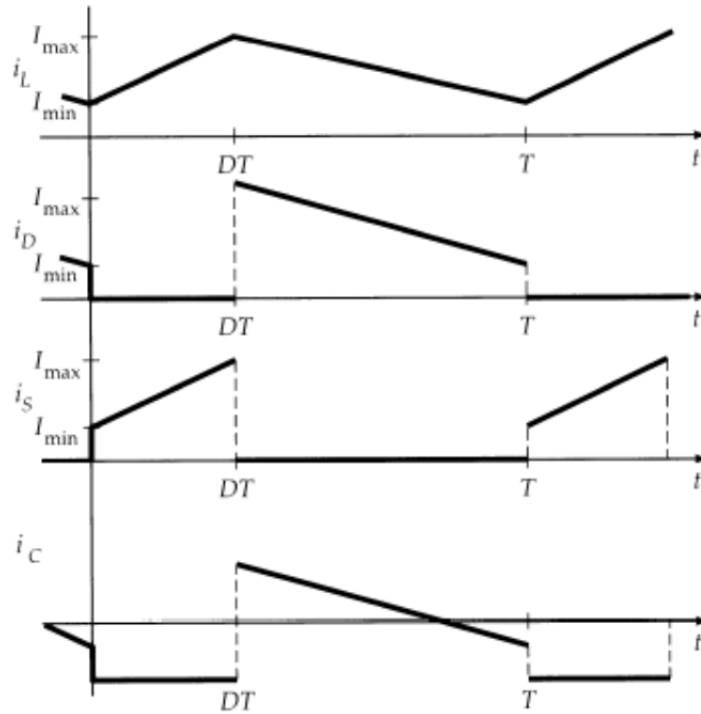


Figure 28. Buck-Boost Component Currents Over Time. Source: [15].

Similarly, the converter looks like a buck converter when the switch is open; therefore, since $E = 0$,

$$v_L = -V_C \quad \text{where} \quad v_C \approx V_C, \quad (8)$$

that equates to

$$L \frac{di_L}{dt} = -V_C. \quad (9)$$

Again by rearranging and integrating, we get

$$I_{\min} - I_{\max} = -\frac{V_C}{L}(1-D)T. \quad (10)$$

Setting these equations equal and cancelling like terms reveals

$$V_C = \left(\frac{D}{1-D} \right) E. \quad (11)$$

This equation makes sense as it has the impact of the duty cycle in the numerator, similar to a buck converter, and in the denominator, similar to a boost converter. From this equation, it is clear that unity gain is achieved when $D = 0.5$. If $D < 0.5$, the circuit operates in buck mode, and if $D > 0.5$ it operates in boost mode. As with the boost converter, careful consideration must be paid to the range of the duty cycle so as not to attempt too much boost that will harm the circuit or cause unpredictable response; therefore, it is generally recommended that the duty cycle remain $0.33 \leq D \leq 0.67$ for a gain range of $0.5 \leq V_C / E \leq 2.00$.

As the critical energy storage device, the inductor must be appropriately sized to ensure CCM. The smallest value of conductance that maintains CCM is called the “critical inductance.” To solve for this value, first the maximum and minimum currents must be determined. We have

$$P_{in} = 0.5(I_{\max} + I_{\min})DE \quad (12)$$

and

$$P_{out} = \frac{V_C^2}{R}. \quad (13)$$

Equating these two powers, we get

$$0.5(I_{\max} + I_{\min})DE = \frac{V_C^2}{R}, \quad (14)$$

and substituting (11), we get

$$\begin{aligned} 0.5(I_{\max} + I_{\min})DE &= \left(\frac{D}{1-D} \right)^2 \frac{E^2}{R}, \\ (I_{\max} + I_{\min}) &= \frac{2DE}{R(1-D)^2}. \end{aligned} \quad (15)$$

Substituting (7) for I_{\max} , we get

$$\frac{E}{L}DT + 2I_{\min} = \frac{2DE}{R(1-D)^2}. \quad (16)$$

The maximum and minimum currents are

$$I_{\min} = \frac{DE}{R(1-D)^2} - \frac{EDT}{2L} \quad (17)$$

and

$$I_{\max} = \frac{DE}{R(1-D)^2} + \frac{EDT}{2L}, \quad (18)$$

respectively. The critical inductance is uncovered by setting $I_{\min} = 0$,

$$L_C = \frac{RT}{2}(1-D)^2. \quad (19)$$

An inductance greater than this value maintains I_{\min} above zero and ensures the converter operates in CCM.

The size of the capacitor depends on the acceptable range of f_s ripple and/or transient response of V_C . The desired capacitance, based on acceptable f_s ripple, can be computed from

$$C = \frac{DV_C}{Rf_s\Delta V_C}, \quad (20)$$

where ΔV_C is the acceptable output voltage ripple.

Each converter presented has advantages and disadvantages depending on the application. Buck converters are generally the most efficient and easiest to control; therefore, systems consisting of panels sized to produce a voltage higher than that required by the load typically employ buck converters. In most military applications, scaling systems large enough to meet various load requirements presents a challenge. Furthermore, varying environmental conditions make input voltages unpredictable; therefore, the flexibility of a buck-boost converter to raise or lower the voltage in dynamic systems presents the best option. This ensures maximum power harvesting from the source delivered at parameters required by various loads.

D. CHAPTER SUMMARY

Many factors affect the operation of a photovoltaic system. Types of solar cells, MPPT algorithm, and converter design often depend on the specific application and anticipated environment. Attempting to design a converter to satisfy all possible types of inputs, loads and environments often results in suboptimal performance. Due to unpredictable environments of military deployment, certain constraints are assumed in this project to ensure maximum power transfer during typical operation.

III. MODELING AND EXPERIMENTAL DESIGN

Simulink by Mathworks, Inc. is the computer simulation program used to model actual physical systems. Since future experiments at NPS will include some of these physical systems, the work described in this chapter serves as a precursor to determine optimum granularity of MPPT application. The chapter begins with a description of the various solar panel configurations simulated for the Puma SUAS. The Simulink model of those configurations is also presented. Next, the simulated environmental conditions are discussed. Finally, each component of the system, along with the corresponding Simulink model, is presented to include the solar cell, MPPT, battery, and load.

A. SYSTEM CONFIGURATIONS

The wing and horizontal stabilizer of the Puma AE II SUAS were acquired from a DOD maintenance depot and are depicted in Figure 29.



Figure 29. Puma AE II Wing and Horizontal Stabilizer.

The outer wings are approximately 89 cm long and 19 cm wide at the narrowest point. The total surface area of the outer wings is approximately 2086 cm^2 . The center

wing is approximately 102 cm long and 28 cm wide with a total surface area of 2856 cm²; however, the total usable surface area of the center wing is only 2724 cm² due to area used to mount the wing to the fuselage. The usable surface area of the horizontal stabilizer is approximately 925 cm². The total usable surface area combined is approximately 7821 cm² or 0.7821 m²; therefore, using 15% efficient CIGS cells, the maximum energy production is approximately 117 W at 1000 W/m² irradiance. In order to best preserve the integrity of manufactured connections between individual cells, submodules are applied intact as much as practical, as depicted in Figure 30.

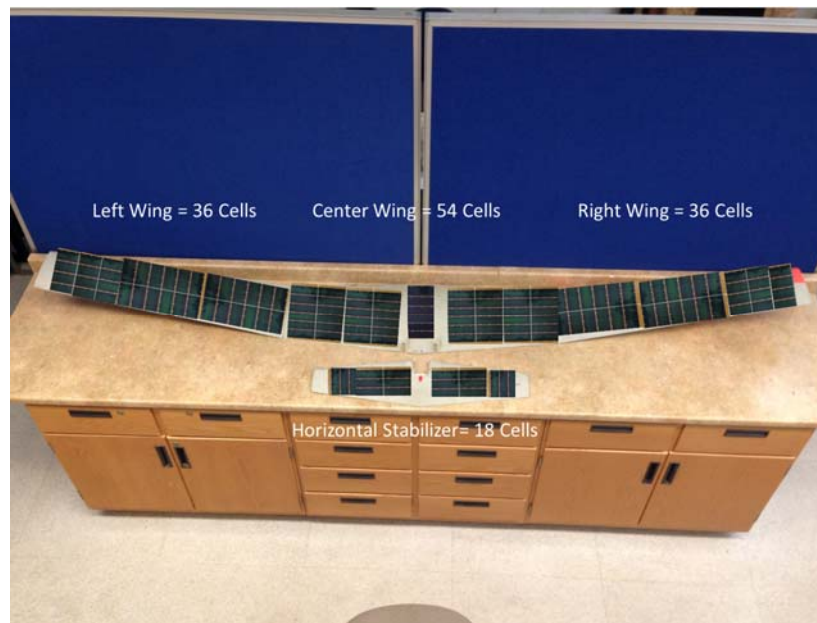


Figure 30. Conceptual Layout of Four Solar Panels on Puma Wing.

The number of solar cells that can be attached to each surface are as follows:

Left Wing: 3 submodules = 36 cells
Center Wing: 4.5 submodules = 54 cells
Right Wing: 3 submodules = 36 cells
Horizontal Stabilizer: 1.5 submodules = 18 cells

This project included three configurations of proposed MPPT converter granularity: 1) MPPT on each surface (i.e., left wing, center wing, right wing, and

horizontal stabilizer); 2) single MPPT prior to battery; 3) no MPPT, or each panel directly connected to battery. The solar panels are connected in parallel in each configuration, thereby creating an electrical bus between each source. The Simulink model of configuration is presented in Figure 31.

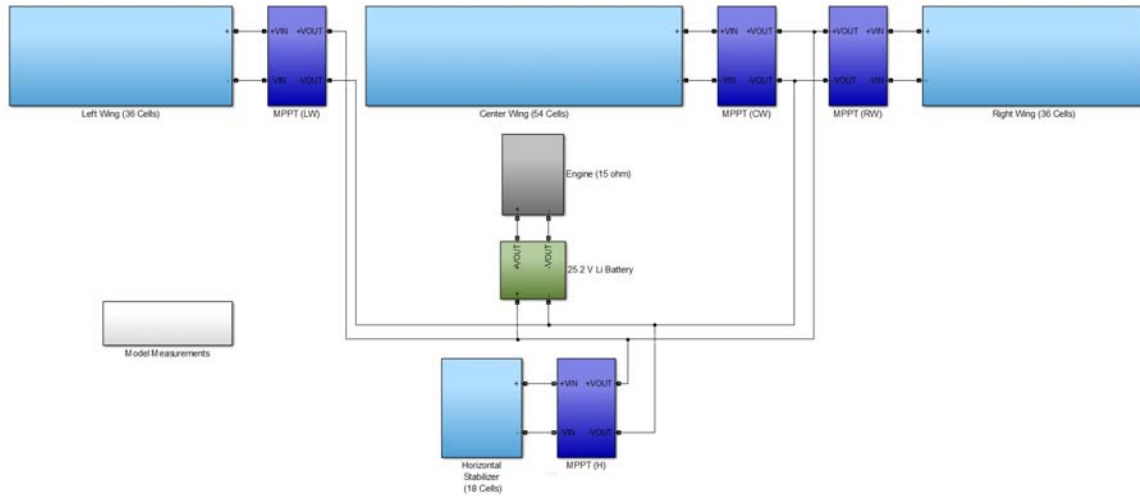


Figure 31. Distributed MPPT Simulink Model.

Depicted in Figure 31, the light blue blocks represent the wings of the SUAS covered in solar cells. The dark blue blocks represent the MPPT. The green block is the Simulink lithium ion battery, and the grey block is a resistive load that simulates the engine. The white block is not connected to the system and is used to collect measurements during simulation. The individual blocks are described in further detail in the next section.

The simulation resulted in negligible power transfer for configurations two and three because the outer wings and horizontal stabilizer were not able to supply power to the centralized converter or battery, respectively; therefore, we determined that the solar panel layout necessary to test configuration 2 and 3 included dividing the main wing into two separate panels instead of three and excluding the horizontal stabilizer, as depicted in Figure 32. The Simulink models of configuration two and three use the same blocks as

configuration one, but the number of solar cells applied to each wing are modified, as presented in Figures 33 and 34.



Figure 32. Conceptual Layout of Two Large Solar Panels on Puma Wing.

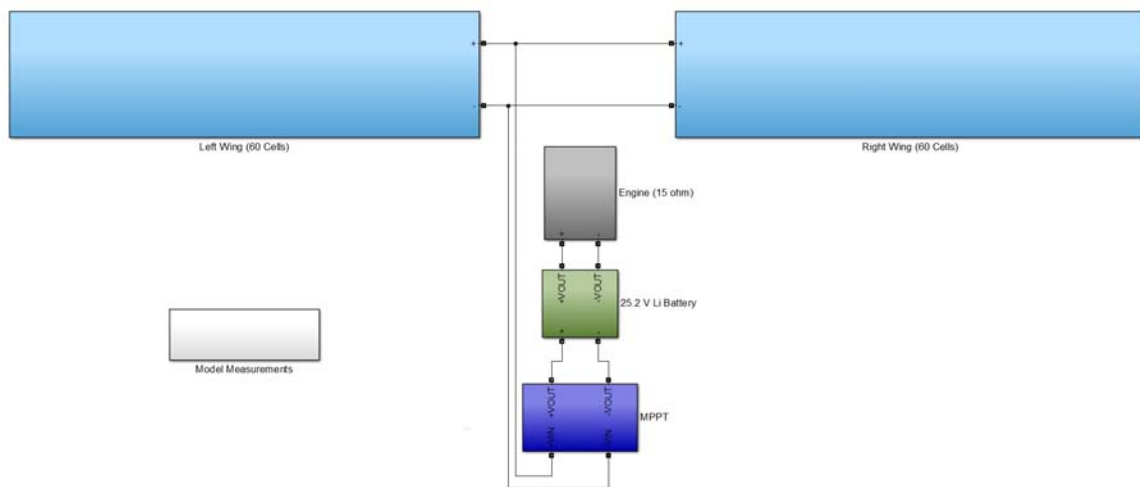


Figure 33. Single MPPT Simulink Model.

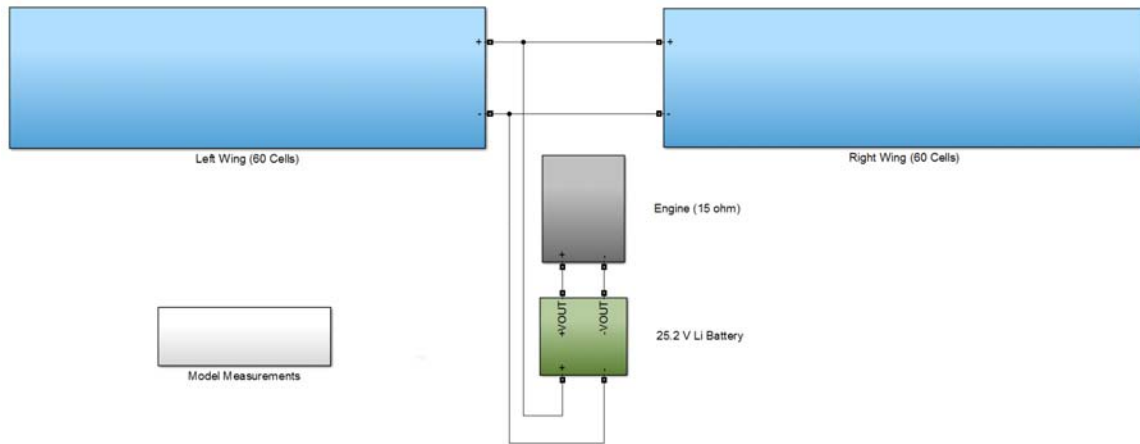


Figure 34. Direct Loaded Simulink Model.

The two large panels each included 60 cells, which provide enough voltage to power the converter or battery in most environmental conditions. Although not optimal, because it resulted in a loss of 24 power generating solar cells, this configuration led to an important conclusion: attempting to cover all surfaces without distributed MPPT does not result in adequate power transfer. It may be possible to cover each surface with smaller solar cells in order to create higher voltage necessary to ensure power transfer; however, this research focused on modeling a system that will actually be constructed. In order to maintain manufacturing integrity, these cells are not divided.

B. ENVIRONMENTAL CONDITIONS

Each configuration was run through a 60-minute test “flight” simulation with varying environmental conditions to determine the system performance. The test flight was divided into three 20-minute intervals that exposed the model to different types of environmental variables. The MATLAB code used to implement these tests is given in the Appendix.

The first interval degraded all solar panels equally. The irradiance was changed from 1000 W/m^2 to 800, 600, 400, and 200 W/m^2 and then incrementally back up to 1000 W/m^2 with each irradiance level lasting for two minutes. This test showcased system

performance for the full range of irradiance values and demonstrated responsiveness during incrementally degrading and improving conditions. In this cycle, the temperature was decreased by five °C for each iteration. The value of temperature change is arbitrary, but a change in temperature is expected with a change in irradiance.

The next 20-minute interval consisted of degrading only one surface for five minutes. For each five-minute sub-interval, the irradiance on only one surface was degraded to 500 W/m², while the other surfaces were kept at 1000 W/m². At the conclusion of five minutes, normal irradiance for that surface resumed and another surface was degraded. For configurations two and three, the left wing and right wing were only degraded for the five-minute interval. This test illustrated the performance of a distributed power conversion system versus a centralized system. The temperature was held constant at 50 °C for this test case.

The final 20-minute interval was designed to expose the system to a periodic degradation of one or more surfaces for short time intervals. This test was meant to simulate the type of sustained periodic degradation a SUAS might experience while flying an oval holding pattern. The degradation values are arbitrary but consistent for all configurations to highlight the system response of different converter granularities. To simulate a one-minute holding turn, the test consists of the left wing degraded to a value of 900 W/m² and the horizontal stabilizer degraded to 800 W/m² for a duration of one minute. The horizontal stabilizer was degraded at a different level because it is obscured laterally and longitudinally during a turn. Then, all panels received 1000 W/m² for one minute to simulate a straight leg of the holding pattern. Next, the right wing and horizontal stabilizer were degraded to simulate a turn in the opposite direction followed by another straight leg. This pattern was repeated for 20 minutes. The temperature was held constant for the entire time. This demonstrated dynamic system response with short duration degradation.

C. SYSTEM COMPONENTS

1. Solar Cells

This project models the CIGS thin-film PowerFlex Solar Cell by Global Solar Energy, Inc. This solar cell was chosen for three reasons: 1) flexibility allows it to conform to the rounded surface of the Puma wing; 2) it provides a relatively high efficiency for its cost; 3) it will be used to build a physical system in future research at the NPS. A picture of one submodule of twelve CIGS cells is presented in Figure 35.

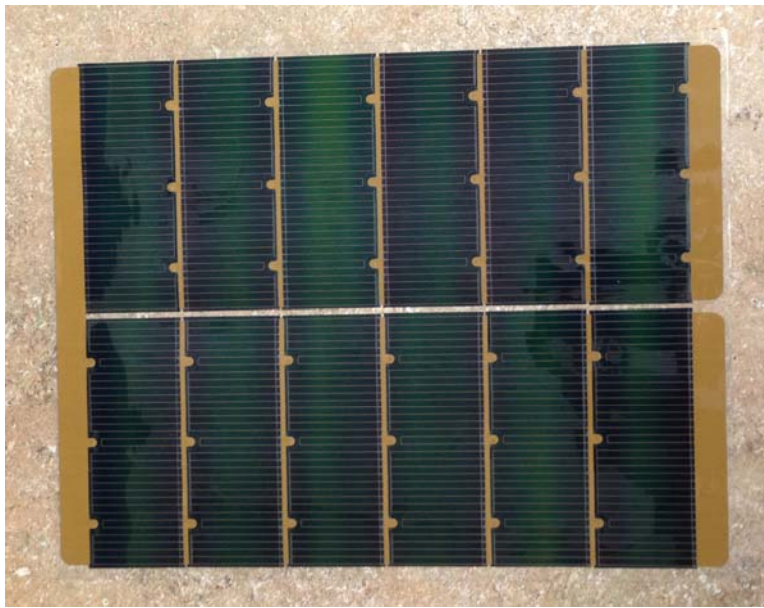


Figure 35. CIGS Thin-Film PowerFlex Solar Cell by Global Solar Energy, Inc.
(Product Number: FG-SM12-11)

The submodules are manufactured as a series connection of 12 solar cells. It is important to maintain the integrity of manufactured connections as much as possible to avoid damaging the cells or introducing errors from poor modifications. The dimensions of each submodule can be seen in Figure 36, and the specifications for the solar submodule are shown in Table 1.

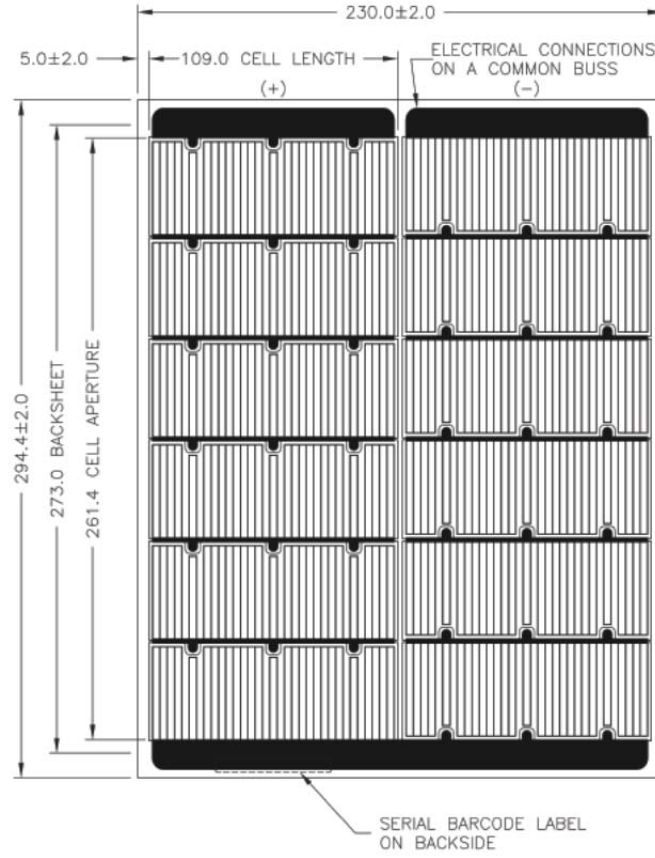


Figure 36. Dimensions for FG-SM12-11: 8.3W (6V) Solar Submodule. Source: [16].

The “aperture area” is the exact surface area of silicon exposed to sunlight. Attachment of the electrical connections to the submodule slightly reduces the area of the current-generating semiconductor material. This area is used to calculate the efficiency by substituting the data presented in Table 1 into (3) to get

$$\eta = \frac{P_{out}}{P_{in}} = \frac{8.3W}{\left(1000 \text{ W/m}^2\right) \left(574 \times 10^{-4} \text{ m}^2\right)} \times 100\% = 14.5\%. \quad (21)$$

Table 1. Product Specifications for FG-SM12-11: 8.3W (6V) Solar Submodule.
Source: [16].

Electrical Characteristics @ STC*	
Rated Power (W)	8.3
Rated Voltage at Maximum Power Point (V)	6.4
Rated Current at Maximum Power Point (A)	1.3
Open Circuit Voltage (V)	8.0
Short Circuit Current (A)	1.4
Physical Characteristics	
Overall Dimensions, mm	230 x 294 x 0.28
Aperture Dimensions, mm	220 x 261
Aperture Area, cm ²	574
Weight, grams	32
Power to Weight Ratio, W/kg	260
Thermal Characteristics	
Temperature Coefficient for Power (%/°C)	-0.43
Temperature Coefficient for Voltage (%/°C)	-0.38
Temperature Coefficient for Voc (%/°C)	-0.33
Temperature Coefficient for Isc (%/°C)	-0.03
Cell Temperature Operating Range (°C)	-40 to 85
Voltage, Open Circuit @ -40°C (V)	10.0

*Electrical Characteristics - tested at Standard Test Conditions (STC): irradiance level 1000W/m², spectrum AM 1.5 and cell temperature 25° C. Tolerance +/-15%.

Furthermore, inputting the data from Table 1 into (2) yields the FF ,

$$FF = \frac{I_{mp} V_{mp}}{I_{sc} V_{OC}} \times 100\% = \frac{(1.3A)(6.4V)}{(1.4A)(8.0V)} \times 100\% = 74.3\%. \quad (22)$$

The preceding two metrics determine the quality of the solar cell. This solar cell has average performance for the current market [6]; however, considering the flexibility, light weight, and low cost characteristics of the cell, it presents the most attractive option for use on a rugged device such as the Puma SUAS.

Using the data from Table 1, we used a MATLAB script to simulate the characteristics of the submodule. This MATLAB program is used to calculate current for each voltage from (1). Then the I-V curve is plotted and compared with Figure 37.

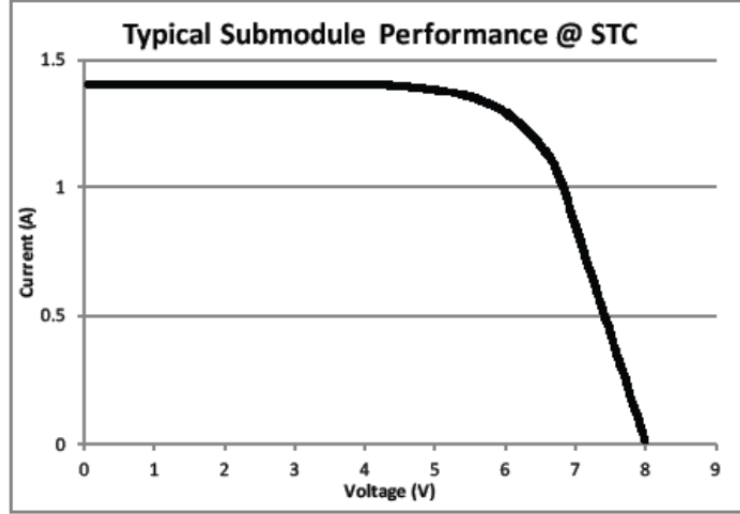


Figure 37. Manufacturer Provided I-V Curve for FG-SM12-11: 8.3W (6V) Solar Submodule. Source: [16].

In order to compute the current from (1), I_o was calculated for standard day conditions. This parameter defines the exponential decay of current as the voltage produced approaches V_{OC} . Using (1), we set I_{total} equal to zero in order to solve for the leakage current. Then, rearranging (1), we get

$$I_o = \frac{I_{SC}}{\left(e^{\frac{qV_{OC}}{nkT_r}} - 1 \right)}, \quad (23)$$

where

$I_{ph} = I_{SC}$, the maximum possible current at standard test conditions (STC);

$V = V_{OC}$, that is the point where $I_{total} = 0$; and

$T_r = 25^\circ \text{C}$, reference temperature at STC.

In order to calculate I_o , the quality factor n must be identified. This information was not provided in the data sheet; therefore, an iterative process was conducted by assigning a quality factor, calculating the leakage current, and then running the MATLAB script to plot the I-V curve. This I-V curve was compared with Figure 31 along with the values for V_{OC} , I_{SC} , V_{MPP} and, I_{MPP} . The quality factor, $n = 2$, yielded the appropriate results, as seen in Figure 38.

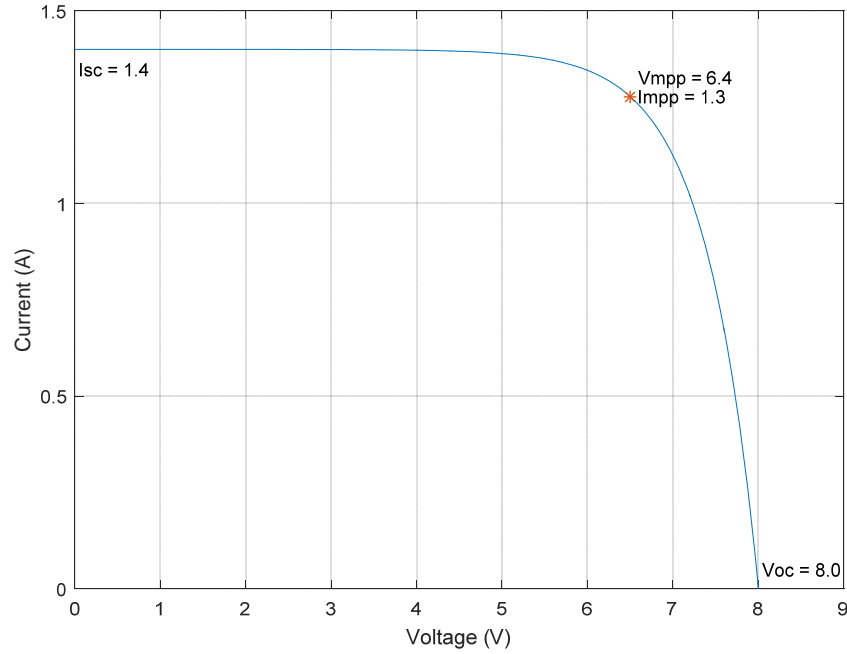


Figure 38. MATLAB-Generated I-V Curve of CIGS Submodule

Next, the leakage current had to be adjusted for temperature. As mentioned in Chapter II, increasing temperature reduces solar cell efficiency. From Table 1, I_{SC} decreases by 0.03 % per $^{\circ}\text{C}$ between the reference temperature (25°C) and the operating temperature. The open-circuit voltage decreases by 0.33 % per $^{\circ}\text{C}$. The leakage current per cell during operation is calculated as

$$I_o = \frac{I_{sc} - (0.0003 \times I_{sc})(T_a - T_r)}{\left(e^{\frac{q(V_{oc} - (0.0033 \times V_{oc})(T_a - T_r))}{nkT_r}} - 1 \right)}, \quad (24)$$

where all values are normalized per cell at STC:

$I_{SC} = 1.4$ A, since series cells have equal current;

$V_{OC} = 0.667$ V per cell;

$q = 1.062 \times 10^{-19}$;

$k = 1.38 \times 10^{-23}$;

$n = 2$;

$T_r = 298.15$ Kelvin, reference temperature at STC (25 °C)); and

T_a = actual temperature of solar cell.

Modeling a single solar cell permits scalability because each surface of the Puma wings has a different number of cells. Also, this makes the model usable for other applications; therefore, determining I_o permitted the calculation of current generated by a single solar cell for a given irradiance. The model presented in Figure 39 is the Simulink model of a solar panel. This corresponds to the contents of the light blue block from Figure 31.

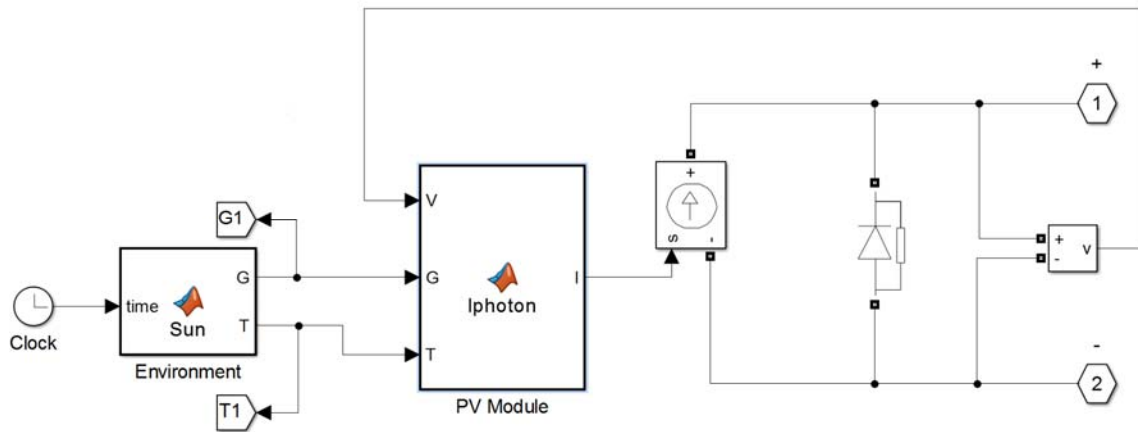


Figure 39. Simulink Model of Solar Panel

The irradiance and temperature throughout the test were generated in the “Environment” function block in accordance with the environmental conditions schedule presented in Section B of this chapter. Using (1), we used a MATLAB script in the “PV

module” function block to generate the current signal for each irradiance and temperature. This current signal drives a Simulink current source. Note that the size of the photovoltaic panel is modified within the “PV Module” function block based on the number of series-connected solar cells. Since the cells are series connected, the current is equal and the voltage additive. The power for an entire panel is just a scalar multiple of the power generated by a single cell; thus, the solar panel is modeled as a current source and a diode, as discussed in Chapter II. The MATLAB code used to simulate the CIGS solar cell is included in the Appendix.

2. MPPT

There are many COTS low-power converters employing MPPT, such as the Genasun GV-4 depicted in Figure 40.

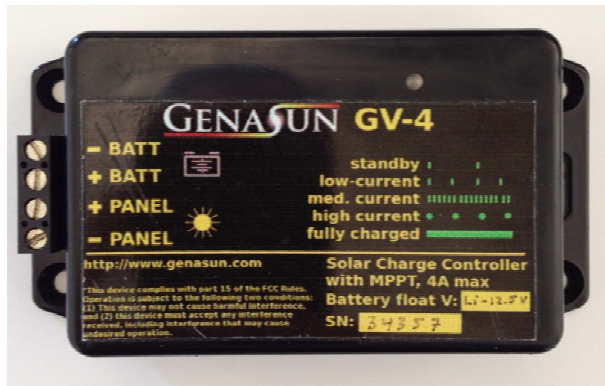


Figure 40. Genasun GV-4 MPPT

Previous research at NPS has used power converters by Genasun, demonstrating solid performance [4]. We did not attempt to model a specific COTS product for this project but instead modeled a generic buck-boost converter in Simulink with similar functionality and performance of COTS low-power converters.

A buck-boost converter was chosen due to its ability to step-up or step-down input voltage. The physical size of the puma wing permits 36 cells on its left and right outer wing and 54 cells in the center wing. Normalizing the submodule open-circuit voltage for a single cell yields $V_{OC}=0.667$ V at STC. Recall that the ratio of V_{MPP}/V_{OC} is

typically between 0.74 and 0.84 [10]; therefore, the operating voltage of the outer wings at STC will likely be between 17.76 and 19.68 V as given by

$$V_{MPP} = 36 \times 0.667 \times (0.74) = 17.76 \text{ V} \quad (25)$$

and

$$V_{MPP} = 36 \times 0.667 \times (0.82) = 19.68 \text{ V}. \quad (26)$$

The center wing operates between 26.64 and 29.52 V. Two separate converters can be designed, one boost and one buck, but when this project is constructed, it will be more economical to have one device that can be used on all surfaces. Furthermore, if portions of the center wing are damaged, causing voltage output degradation below the operating voltage of the battery, a buck converter will be useless and all power generated lost.

Corresponding to the dark blue block of Figure 31, the Simulink design of the MPPT buck-boost converter is shown in Figure 41.

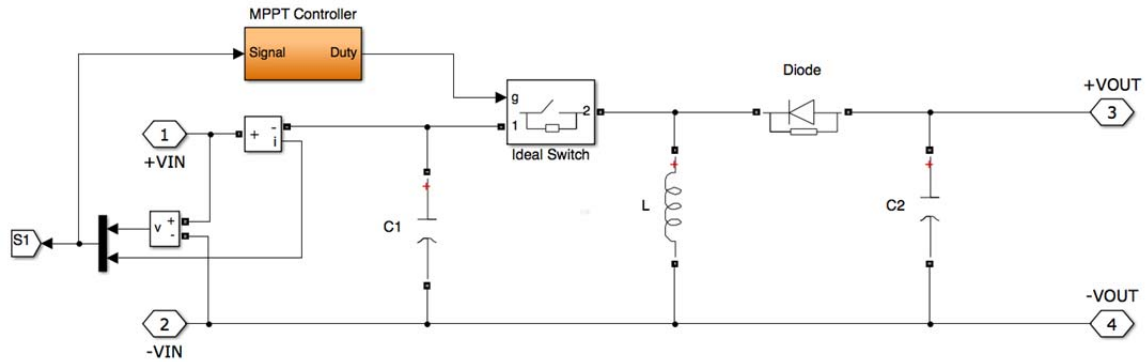


Figure 41. Buck-Boost Converter with MPPT Simulation

A few key differences can be noted between the model presented in Figure 41 and the basic buck-boost converter as shown in Figure 26. First, this model does not include the source and load because they are separate mask blocks in the entire Simulink design. Second, the switch is controlled by an MPPT, represented by the orange block. Finally,

this converter includes a leading capacitor, C_1 , for two reasons: 1) a parallel capacitor must be included with a current source; 2) the capacitor dampens the input voltage waveform, which provides for smoother measurement.

The leading capacitor was sized using an iterative approach to produce a desirable waveform. This capacitor has a value of 10.0 μF . Next, the critical inductance was calculated as

$$L_c = \frac{RT}{2}(1-D)^2 = \frac{(15)(1 \times 10^{-4})}{2}(1-0.415)^2 = 0.256 \text{ mH}, \quad (27)$$

where

$R = 15 \Omega$, which is the average resistive load to be discussed later;

$T = 1/f_s$, the period of the 10 kHz switching frequency; and

$D = \text{duty cycle}$.

The inductor was oversized to 1.0 mH to ensure the converter would operate in CCM.

The duty cycle was calculated for the absolute minimum value, yielding the largest inductance that could possibly be needed. The absolute minimum duty cycle occurs if the largest panel is operating near its largest voltage V_{OC} . The center wing has 54 solar cells, yielding a $V_{OC} = 36.02 \text{ V}$, and the battery operates a constant 25.6 V per the data sheet. By rearranging (11), we get the duty cycle

$$D = \frac{V_c}{V_c + E} = \frac{25.6}{25.6 + 36.02} = 0.415. \quad (28)$$

Next, we determined that output ripple voltage should not exceed 0.1 V; therefore, the output capacitor was sized by

$$C = \frac{DV_c}{Rf_s \Delta V_c} = \frac{(0.415)(25.6)}{(15)(1 \times 10^4)(0.1)} = 0.708 \text{ mF}. \quad (29)$$

This capacitor is larger than required, presumably because of the low impedance of the battery, and a 10.0 μF capacitor proved sufficient.

Finally, an ideal switch (no losses) was chosen for simplicity and to maintain a high level of efficiency for the converter. This switch is driven by a 10-kHz Boolean pulsed-width modulation signal. The duration of the “on” or “off” pulse is determined by modulating a triangle wave with a duty cycle generated by a MATLAB function block, as shown in Figure 42. Inputs to this function block include the voltage and current from the source side of the converter in Figure 41 and a clock signal. The function block executes the P&O algorithm at a fixed interval to reduce processing time and to collect samples of averaged transients. The MATLAB function used to control the duty cycle with the perturb and observe algorithm is included in the Appendix. The model presented in Figure 42 illustrates the details contained in the orange “MPPT Controller” block from Figure 41.

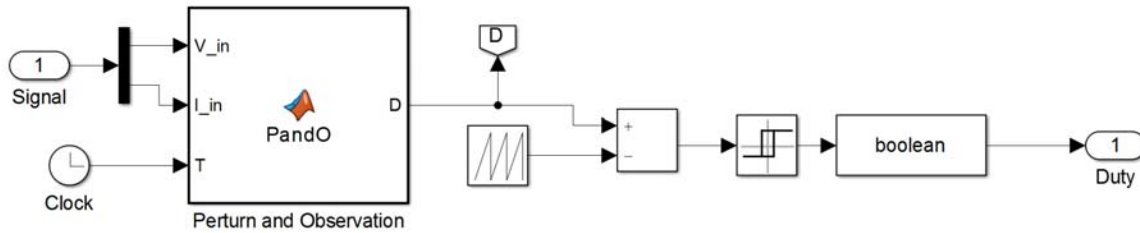


Figure 42. Model of MPPT Controller Displayed in Figure 35

The intent of this design was not to design a converter nor to mimic a COTS converter but to model functionality. COTS converters use various sized components and layouts that may differ from this design. At 95% efficiency, this model slightly underperforms comparable COTS products; however, the model is sufficient to reinforce the concepts presented in this research.

3. Battery / Load

Modeling the actual battery used on the Puma AE II SUAS, as seen in Figure 43, is beyond the scope of this research; therefore, the most important parameters from the datasheet were inputted into Simulink’s standard lithium ion battery model to provide an adequate representation of the physical system. From the SUAS manual, this lithium ion

battery has a fully charged voltage of 25.2 V and a capacity of 13.5 Ah [17]. Once input into the Simulink model, the result was a nominal voltage of 21.7 V.

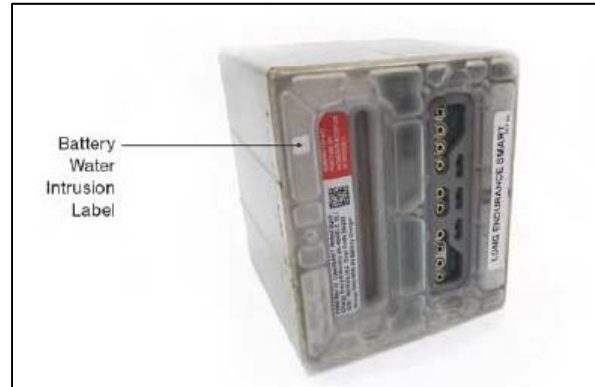


Figure 43. Puma AE II Lithium Ion Battery. Source: [17].

Furthermore, the state of charge was set to 75% to ensure the battery would accept power transfer from the converter during simulation. The battery terminals are inverted due to the power inversion nature of the buck-boost converter, as depicted in Figure 44. The remaining parameters of the Simulink model remained untouched.

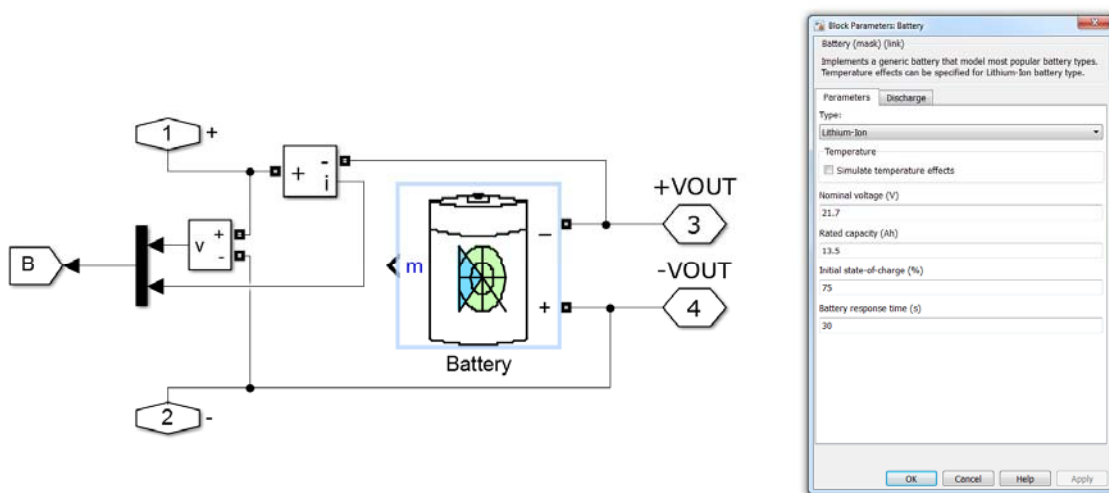


Figure 44. Modified Simulink Lithium Ion Battery Model

Because this project was unable to acquire an entire Puma system, including a battery and engine, experimental load data was not available; however, previous NPS research captured load data for a similar system, the RQ-11B Raven SUAS [18]. Actual flights were conducted and throttle position recorded for the duration of the flight. Data from all flights were compiled to determine throttle position for a typical flight, as depicted in Figure 45. Next, the Raven engine was powered while measuring current and voltage output at each throttle position. Based on the typical flight, the throttle averaged approximately 40% for most of the flight, which equates to 24.55 V and 1.79 A. An assumption was made that the load can be considered resistive, typically operating between 10 and 15 Ω . The Puma engine is modeled as a 15 Ω resistive load.

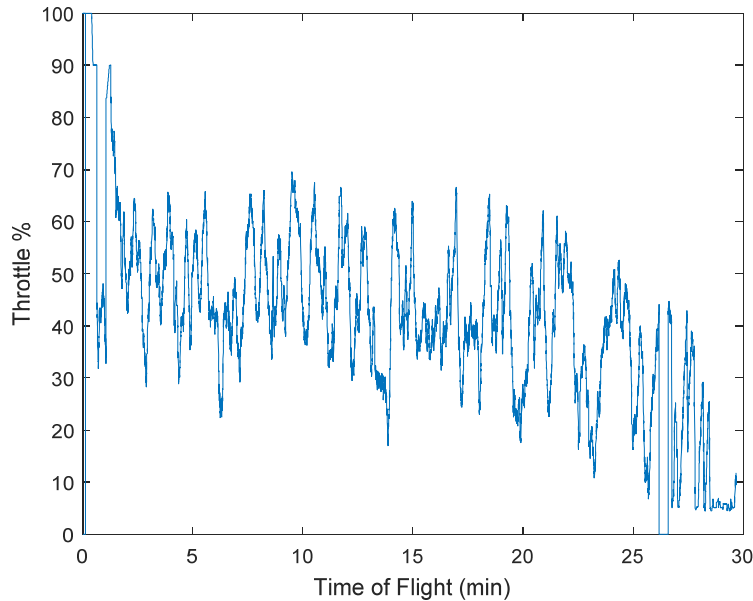


Figure 45. Throttle Position of Typical Raven Flight. Source: [18].

D. CHAPTER SUMMARY

In this chapter, the design and model of the various solar panel configurations on the Puma, the simulated environmental conditions, and the individual components of the system were presented. This model was intentionally designed to simulate general functionality instead of specific components; therefore, it can be easily modified for different applications, different types of solar cells, or different SUAS configurations.

IV. RESULTS

A comparative analysis of power transfer during simulation for each solar panel configuration on the Puma SUAS is provided in this chapter. For each configuration, expected power generation by the combination of all solar panels is presented as a baseline for comparison. Next, the actual power generation and power transfer is analyzed to validate the model. Then, total system efficiency is compared for each configuration. Finally, the system performance is analyzed for each configuration under the various environmental test conditions.

A. THEORETICAL VERSUS EXPERIMENTAL POWER TRANSFER

1. Configuration One: Four Distributed MPPT

The equations presented in Chapter III were used with a MATLAB script to determine theoretical performance of the solar cells. The theoretical P-V curves for each panel on configuration one is presented in Figure 46.

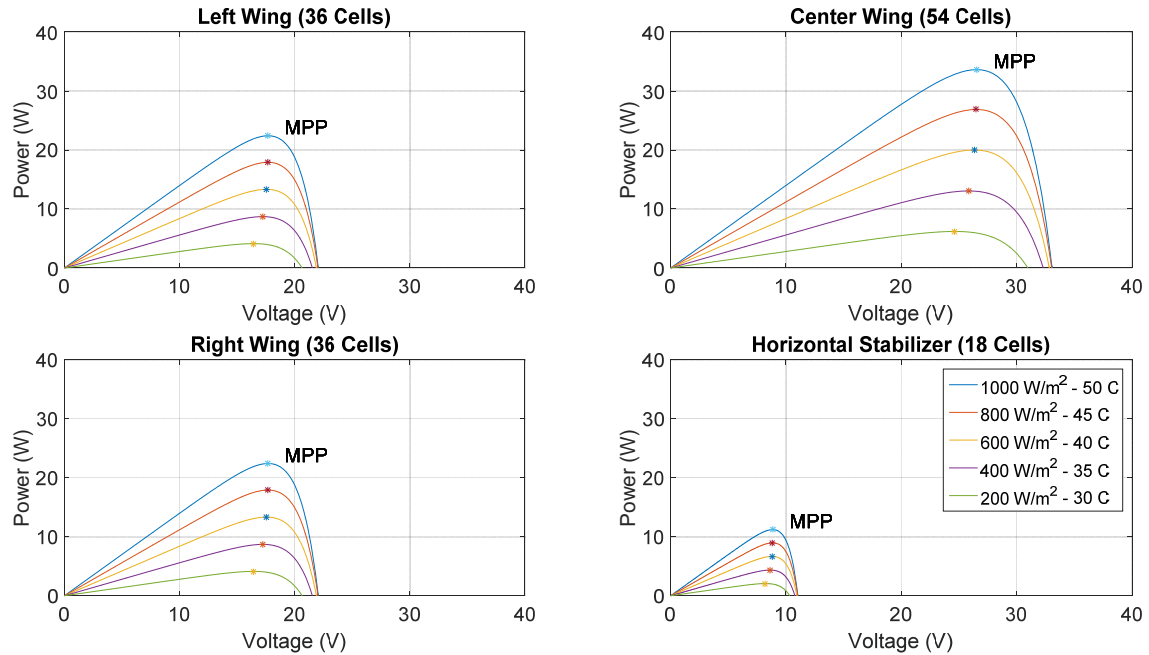


Figure 46. Configuration One Individual Wing P-V Curves for Varying Environmental Conditions

Since the focus of this work is power transfer, the I-V curves are not required, and only the P-V curves are presented to determine the maximum possible power generated for each environmental condition of the first test condition. From the data, the left and right wings are capable of producing approximately 24.3 W, the center wing is capable of producing 36.6 W, and the horizontal stabilizer is capable of producing 11.2 W. Combining these results yields a total maximum power of 96.4 W at 1000 W/m² and 50 °C for configuration one.

The result of the test simulation for each surface of configuration one is shown in Figure 47, annotated with the three environmental condition test cases used for all three configurations. In test case one, irradiance and temperature are degraded for two minutes each across all surfaces. In test case two, only irradiance is degraded for five minutes on only one surface at a time. Test case three is a simulation of a holding pattern, where an outer wing and the horizontal stabilizer are periodically degraded every other minute. The blue line, representing the power generated by the left wing, is sometimes obscured by the right wing's line due to identical power generation.

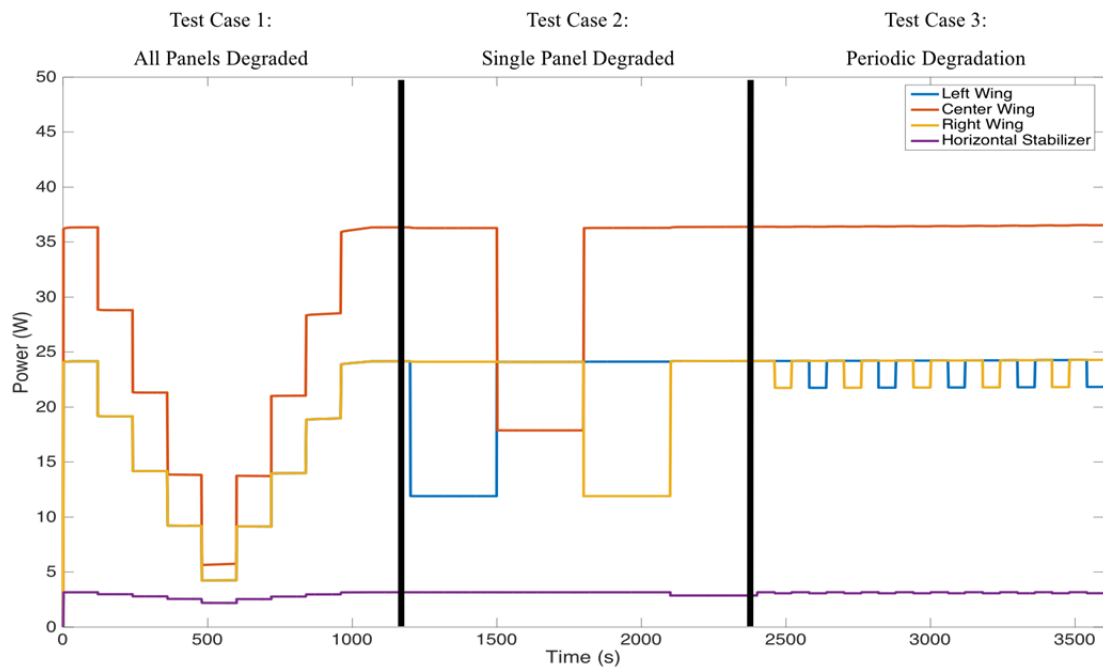


Figure 47. Individual Power Generated by Each Surface for 60-minute Flight of Four-Panel SUAS with Four Distributed MPPTs (Configuration One)

It appears that each of the MPPTs for the left wing, right wing and center wing worked well. The left and right wing generated 24.1 W, during peak environmental conditions of 1000 W/m^2 and 50°C . For the same environmental conditions, the center wing produced 36.2 W; therefore, each corresponding MPPT tracked within 99% of possible power generation. The MPPT for the horizontal stabilizer did not perform as advertised, likely due to the low power generation of the surface. From Figure 46, the horizontal stabilizer is capable of producing just over 11 W during peak environmental conditions, but the simulation produced less than four W.

Combining the results from each surface, the total power generated by the solar panels was 87.5 W at 1000 W/m^2 and 50°C , as illustrated by the blue line in Figure 48. The total power transferred to the battery was 82.7 W, represented by the red line in Figure 48. As stated in Chapter III, applying a single MPPT or no MPPT to the four-panel configuration resulted in negligible power transfer; therefore, the system response is Figure 48 presents the best granularity of MPPT for the four-panel array.

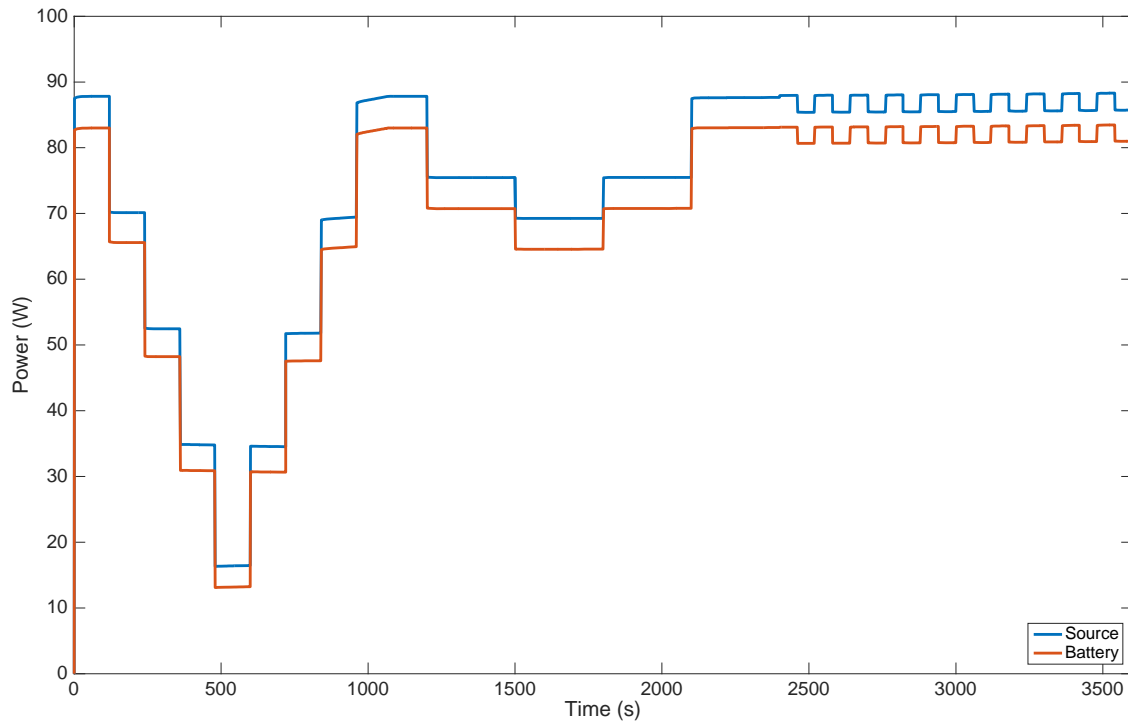


Figure 48. Power Transfer for 60-minute Flight of Four-Panel SUAS with Four Distributed MPPTs (Configuration One)

2. Configuration Two: Single MPPT

Since a single converter (or direct connection) of the four-panel configuration produced negligible power transfer, configuration two includes two large surfaces on the left and right wings of the SUAS, respectively. The theoretical power generation of these surfaces is presented in Figure 49.

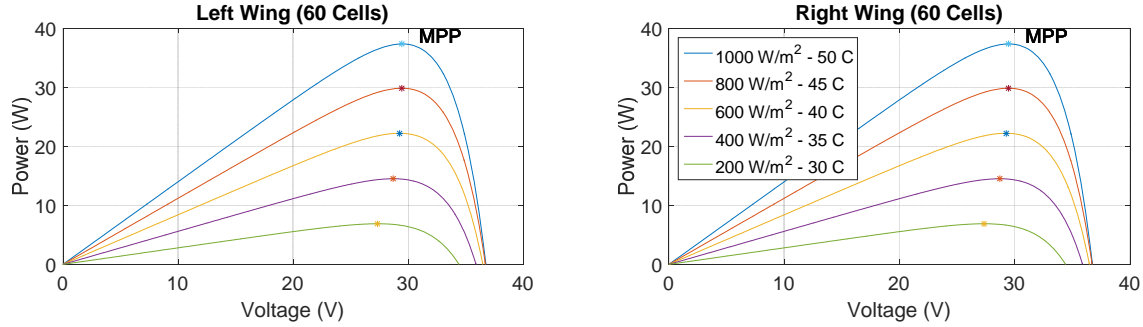


Figure 49. Configuration Two and Three, P-V Curves for Varying Environmental Conditions

From the data, the theoretical maximum power at an irradiance of 1000 W/m² and a temperature of 50 °C is 37.4 W for each wing. This results in a total theoretical power of 74.8 W for configuration two. Comparing the theoretical maximum power to the results of the simulation presented in Figure 50, the single MPPT performed well. At 1000 W/m² and 50 °C, the simulation results show a generated power of 72.9 W with 70.0 W transferred to the battery; therefore, the single MPPT tracked the MPP at approximately 98% of the theoretical maximum power generation of the entire array.

Even during environmental test cases two and three, when only one surface is degraded, the single MPPT was able to remain within 98% of the MPP for the system. Only the irradiance was degraded, which has a drastic impact on current generation but only minimum effect on voltage. Although the power generation of the degraded panel was reduced by half, at 500 W/m² for environmental test case two, the voltage remained large enough to supply the diminished current to the battery. Since the panels are

connected in parallel, the MPPT did not sense much degradation in voltage and adjusted the duty cycle to maximize power generation by both panels.

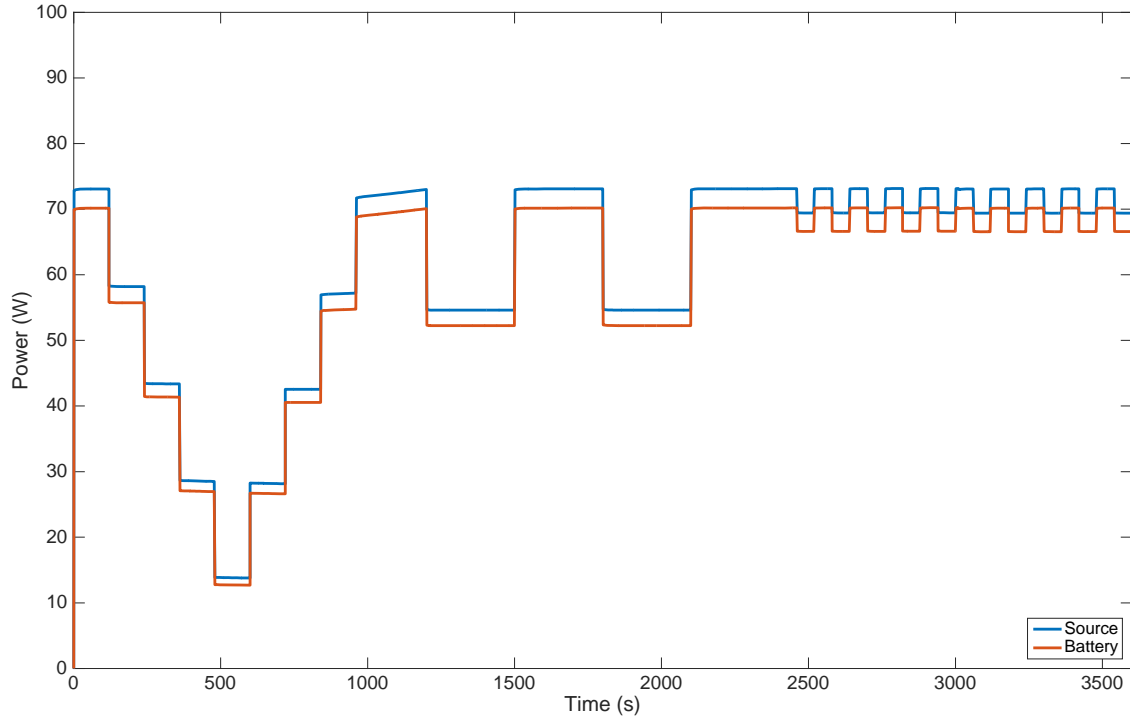


Figure 50. Power Transfer for 60-minute Flight of Two-Panel SUAS with a Single Centralized MPPT (Configuration Two)

3. Configuration Three: No MPPT

The simulation results for configuration three are presented in Figure 51. Since the solar panel layout is identical, the total possible power generation for configuration three is the same as configuration two. The only change for this layout is that the power generated equals the power transferred because the solar panels are directly connected to the battery. The total power curve in Figure 51 represents both power production and power transfer of the system. Interestingly, the power produced by this system at peak conditions is less than that of configuration two, at only 71.7 W at 1000 W/m² and 50 °C, but more power is supplied to the battery because there are no insertion losses introduced by an MPPT.

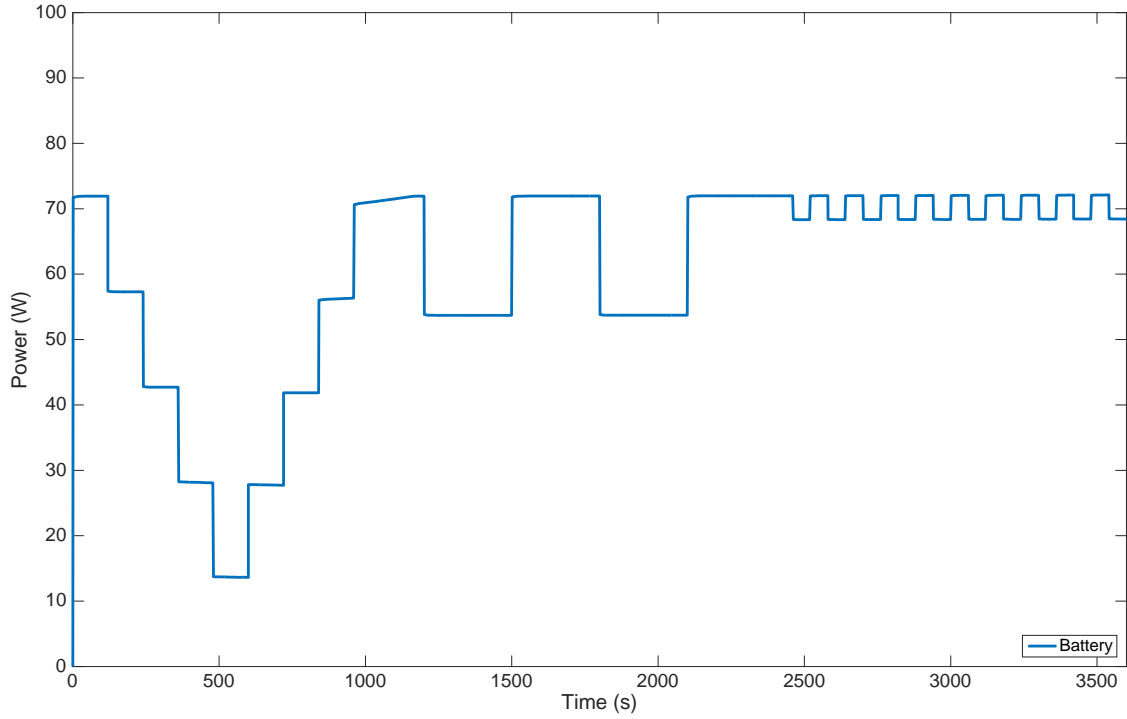


Figure 51. Power Transfer for 60-minute Flight of Two-Panel SUAS with No MPPT (Configuration Three)

Thus, far, only the power generated during peak environmental conditions, 1000 W/m^2 irradiance and 50°C temperature, has been used to analyze the performance of each configuration. Using this single set of environmental parameters permitted comparison of simulation performance to theoretical values while keeping the data presented during the discussion simple. The results presented in Figures 48, 50, and 51 demonstrate that the simulation of each configuration was near theoretical values for the range of environmental conditions generated by test case one. Furthermore, those plots demonstrate the MPPT performance in tracking the MPP for both continually degrading conditions and improving conditions. The demonstrated performance indicates robustness of the system by providing maximum power transfer during all operating environments.

B. EFFICIENCY COMPARISON

Comparing the efficiencies of the different configurations provides a useful analysis for determining the optimum granularity of MPPT. The total system efficiency is

defined as the ratio of power transferred to power generated, or $P_{source}/P_{battery} \times 100\%$. The total system efficiency is different from MPPT efficiency. As mentioned in Section A, the MPPT efficiency was approximately 99% for configuration one and 98% for configuration two; however, the total system efficiencies were much different, as displayed in Figure 52.

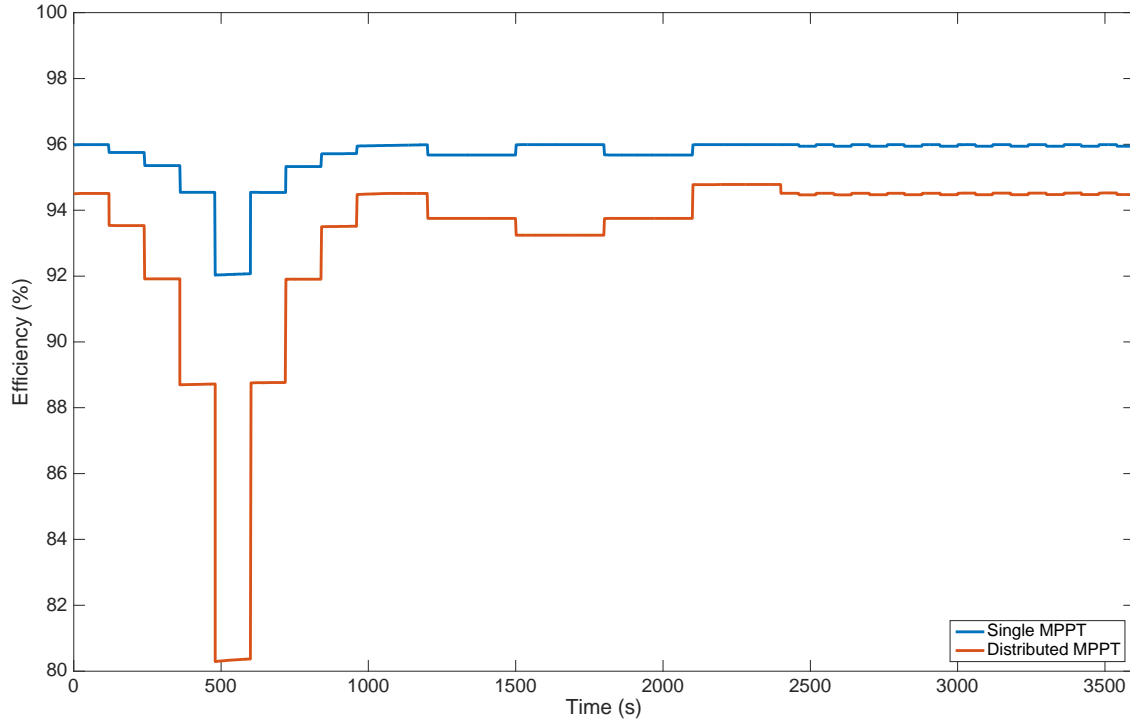


Figure 52. Comparison of Energy Transfer Efficiency between Distributed and a Single Centralized MPPT

The total system efficiency for configuration one was 94.5% when exposed to 1000 W/m^2 irradiance and 50°C temperature, represented by the orange line in Figure 52. The total system efficiency for configuration two was 96% for the same environmental conditions. Note that the system efficiency for configuration three was 100%, since power generated equals power transferred. From the plot in Figure 52 (between 250 s and 750 s), it is apparent that efficiency decreases significantly for a reduction in irradiance and temperature. This indicates that the insertion losses, power lost in MPPT, are relatively stable. In other words, the magnitude of power lost in tracking the MPP is the

same regardless of the magnitude of power generated. For instance, the panels in configuration one generate approximately 89 W at 1000 W/m^2 and 50°C , and the power lost is 4.8 W. At 200 W/m^2 and 30°C only 16 W is generated, but the power lost is 3.2 W. The significant reduction in efficiency of configuration one versus configuration two is due to the additive effect of the four MPPTs.

C. CONFIGURATION COMPARISON FOR EACH TEST CASE

In this section, the system performance for each configuration during each test case is compared. A detailed comparison of system performance for environmental condition one is presented in Table 2.

Table 2. Configuration Performance Comparison for Test Case One

All Surfaces Degraded	Config. 1	Config. 2	Config. 3
1000 W/m^2 5°C			
P_{source} (W)	87.5	72.9	71.7
P_{battery} (W)	82.7	70.0	71.7
Efficiency (%)	94.5	96.0	100
800 W/m^2 45°C			
P_{source} (W)	70.2	58.3	57.4
P_{battery} (W)	65.7	55.8	57.4
Efficiency (%)	93.5	95.8	100
600 W/m^2 4°C			
P_{source} (W)	52.5	43.4	42.7
P_{battery} (W)	48.2	41.4	42.7
Efficiency (%)	91.9	95.4	100
400 W/m^2 35°C			
P_{source} (W)	34.9	28.7	28.2
P_{battery} (W)	30.9	27.1	28.2
Efficiency (%)	88.7	94.5	100
200 W/m^2 3°C			
P_{source} (W)	16.4	13.9	13.7
P_{battery} (W)	13.1	12.8	13.7
Efficiency (%)	80.3	92.0	100

The data in Table 2 illustrates three important points. First, maximum power is delivered to the battery in configuration one. Of course, configuration one includes more solar cells. A single MPPT or directly connected array would not deliver power to the

battery, leaving configuration one as the best option for maximum power generation and transfer. Secondly, the total system efficiency for configuration two is higher than that of configuration one. Again, insertion losses are additive for the four MPPT configurations. Third, directly connecting the larger solar panels for configuration three results in more power transferred because of no insertion losses.

Next, the performance of the three configurations during environmental condition two are compared in Table 3. In this test condition, only one surface is degraded at a time with 500 W/m^2 irradiance and at a temperature of 50°C .

Table 3. Configuration Performance Comparison for Test Case Two

Single Surface Degraded	Config. 1	Config. 2	Config. 3
Left Wing - 500 W/m^2 50°C			
P_{source} (W)	75.5	54.7	53.7
P_{battery} (W)	70.8	52.3	53.7
Efficiency (%)	93.8	95.7	100
Right Wing - 500 W/m^2 50°C			
P_{source} (W)	75.5	54.7	53.7
P_{battery} (W)	70.8	52.3	53.7
Efficiency (%)	93.8	95.7	100
Center Wing - 500 W/m^2 50°C			
P_{source} (W)	69.3		
P_{battery} (W)	64.6		
Efficiency (%)	93.2		
Horizontal Stab. - 500 W/m^2 50°C			
P_{source} (W)	87.5		
P_{battery} (W)	83.0		
Efficiency (%)	94.8		

The simulation results for all three configurations are similar to those presented in Table 2. The power generated, power transferred, and efficiency all decrease slightly as each surface is degraded. Furthermore, the MPPT continues to track the MPP to permit nearly maximum power generation. Configuration three still delivers more power to the battery, although less power is generated, which means that insertion losses of the single MPPT in configuration two are greater than the additional power generated. The most

interesting observation from this test condition is that the efficiency remains high when only the horizontal stabilizer is degraded. As the smallest surface area, the horizontal stabilizer has the smallest impact on power generation. The total system will perform at high efficiency with or without the power generated by this surface. This observation reinforces the central point of this project: applying distributed MPPT results in increased system performance when one or more surfaces are degraded.

The final performance comparison for each configuration during environmental condition three is presented in Table 4.

Table 4. Configuration Performance Comparison for Test Case Three

Turn: Outer Wing-900 W/m² 50 °C Horiz. Stab.- 800 W/m² 50 °C			
Straight Leg: All surfaces - 1000 W/m² 50 °C	Config. 1	Config. 2	Config. 3
Turn			
P _{source} (W)	85.4	69.5	68.3
P _{battery} (W)	80.7	66.6	68.3
Efficiency (%)	94.5	95.9	100
Straight Leg			
P _{source} (W)	87.9	73.1	72.0
P _{battery} (W)	83.1	70.2	72.0
Efficiency (%)	94.5	96.0	100

Environmental test condition three represents the most likely “real-world” test condition. The primary mission of most SUAS is to loiter over an objective or intended route to provide persistent intelligence, surveillance, and reconnaissance. The flight profile during this loiter period is typically an elliptical holding pattern; therefore, it is feasible that one or more of the surfaces of the SUAS may experience degraded irradiance in a periodic manner depending on the sun position. The data does not reveal any new significant performance characteristics. The system remains consistent throughout the periodic test condition, which allows for extrapolation of this performance across a longer duration flight event. If this is representative of a typical flight profile,

this performance data will help make conclusions on the optimum granularity of MPPT and expected return on investment of the system in terms of increased endurance.

D. CHAPTER SUMMARY

In this chapter, a comparative analysis of the performance of three configurations (distributed MPPT, single MPPT, and no MPPT) facilitated determination of the optimum granularity of MPPTs on a low power photovoltaic array. Comparing theoretically possible power generation versus power generated by the model highlights the MPPT efficiency and validates the model as functionally comparable to COTS converters. The total power transfer and system efficiency for each configuration highlights system performance for determination of MPPT granularity. Finally, analyzing system performance for each test condition illustrates the robustness of this design and a comparative view of system performance for many operating environments.

THIS PAGE INTENTIONALLY LEFT BLANK

V. CONCLUSION

A. OPTIMAL GRANULARITY

The optimal granularity of MPPT is dependent on the application. For maximum power delivered to the battery on the Puma SUAS in order to extend flight time, configuration one presents the optimal granularity. This conclusion is based on the simple comparison of power delivered to the battery by each configuration. In configuration one, 82.7 W was delivered to the battery during peak conditions. In configuration two, 70.0W and for configuration three 71.7 W was delivered. For configuration one, attempting to use a single MPPT or directly connecting the solar panels to the battery resulted in negligible power transfer. In order to reduce the number of MPPTs required, the layouts of configurations two and three resulted in less surface area coverage. By utilizing distributed MPPT, more surface area could be covered, generating more power and resulting in more power supplied to the battery.

Experimental data was not available for the electrical load of the Puma engine. AeroVironment, Inc. advertises 210 minutes of flight time for the Puma AE II SUAS [17]. Assuming the battery does not operate below 20% charge and neglecting the added weight and aerodynamic effects of solar cells and MPPT, the Puma engine can be expected to operate at approximately 24 V and approximately 3.1 A. This equates to 74.4 W required to power the Puma. In peak environmental conditions, configuration two or three provides enough power to operate the Puma nearly indefinitely; however, military operations do not occur only during perfect weather. Clouds, dust, or other factors can also negatively influence the performance of the system. In this case, the additional power provided by configuration one may prove vital for mission success.

For other SUAS or other solar augmented applications, weight, space, or cost may be a primary constraint. In these cases, the additional power gained by distributed MPPT may not be worth sacrificing another primary constraint. Interestingly, configuration three outperformed configuration two for every test condition. Again, this is because the voltage produced by the two panels of these configurations remained large

enough to supply current to the battery. Coincidentally, the size of these panels resulted in a voltage at the maximum power point relatively close to the voltage threshold of the battery. In other words, the MPPT of configuration two may have permitted better power generation by the wings, but those gains were negated by the insertion losses associated with the MPPT operation. If weight, space, or cost outweighed the added power of configuration one for the Puma, configuration three would be the best layout. Since each application is different, balancing the constraints, mission, and operating environments of that specific application is necessary to determine optimum MPPT granularity.

B. COST ANALYSIS (SYSTEM, MAINTENANCE, TACTICAL)

Cost is always a constraint for military equipment. As stewards of taxpayer resources, the DOD strives to satisfy mission requirements in the most affordable manner; therefore, cost also plays a role in defining the optimum granularity of MPPT.

During TechCon 2017, hosted by the Crusier Consortium at the Naval Postgraduate School, Mr. Rob Parenti, a senior product engineer with Alta Devices, Inc., stated that his company continually works to provide solar energy augmentation for SUAS. The solar cell they use for these projects provides 25–26% efficiency and costs approximately \$100 per W of generated electric power [19]. Assuming the same aperture area as covered as configuration one by a 26% efficient cell, we expect the power generation by Alta cells to be approximately 179 W. The solar cells alone would cost \$17,900.

In contrast, the 15% efficient CIGS cell by Global Solar Energy, Inc. costs approximately \$2.00 per W, based on purchase order and performance specifications provided in the datasheet [16]. The 144 cells included in configuration one are capable of generating 100 W at STC, for a total cost of \$200. This power was calculated by normalizing the maximum power specification from the datasheet yielding 0.692 W/cell. In Chapter IV, the maximum power presented is only 96.4 W, not 100 W, but this is due to a more realistic operating temperature of 50 °C. Regardless, the datasheet specification is the metric used to determine cost.

Assuming MPPT, construction costs, etc., are equal, the equipment presented in this project can supply enough electric power to provide nearly indefinite daytime endurance to the Puma AE II SUAS for approximately 1.12% of the cost of the Alta Devices, Inc. equivalent. Maintenance expenses must also be included in this analysis. The nature of SUAS operation is inherently rough because the aircraft conducts a controlled crash during retrieval. Plus, the system is disassembled for transport and possibly transported in hostile environmental conditions. The wing and horizontal stabilizer, presented in Chapter III, was acquired from depot maintenance and included significant puncture holes, surface gouges and scratches; therefore, covering the surface in expensive high efficiency solar cells may prove financially irresponsible. If mission requirements can be achieved at a fraction of the cost, perhaps the solar cells can be determined consumable and stripped and replaced during depot maintenance.

Of course, this is a wave top analysis based purely on advertised efficiencies of statically tested solar cells and approximate engine load performance. Actually mounting solar cells may incur added costs and decrease efficiencies. Furthermore, the system needs to be mounted on an actual SUAS and flown to determine engine performance with the added weight of solar cells and MPPT.

Additional electric load in the form of optical sensors and communications equipment is another consideration not included in this analysis. This type of equipment adds significant electric power requirements. The system proposed in this research can supply enough power to extend the endurance of the engine; however, if extended endurance of the total system is required, a higher efficiency cell may be necessary to satisfy the mission objectives.

C. RECOMMENDATIONS FOR FUTURE WORK

During this project, a few opportunities for further research became apparent.

1. Test with Hardware

The first opportunity for extending this research is to build the system with actual hardware. Researchers in the Electrical and Computer Engineering Department at NPS

are attempting to gather data for configurations two and three. As shown, configuration one provides the most power to the system, and building configuration one with CIGS cells would help validate this research. Furthermore, for any solar augmented SUAS project, the ultimate test occurs during flight conditions. This entails an extensive approval process, but hopefully leveraging the results of this thesis will provide the necessary justification.

2. Design/Build Solar Cell with MPPT Integrated Circuit

The MPPT presented in this project models the functionality of a COTS power converter. Most 100-W power converters are not designed with size or weight as a primary concern. The MPPT algorithm is usually implemented via microchip, but the inductors and other elements are relatively large and heavy. Reducing the size of the MPPT would be an excellent research area. Furthermore, if most of the components could be integrated on a chip, perhaps MPPT could be implemented at the submodule or even cell level.

3. Centralized Micro-Controller for Dynamic Logic

The next area for continued research may include implementing a single micro-controller which functions like distributed MPPT. Similar to the TEODI concept presented in Chapter II, a device such as an Arduino could accept inputs from each surface and make adjustments to maximize power transfer using a single centralized device. This device may also be able to dynamically share passive energy storage devices like inductors and capacitors to further reduce the components required.

4. Incorporate Telemetry Data to Better Refine Model

Finally, incorporating actual flight information into this type of Simulink model can enhance the predictive capacity in the design stage. Sun angles, temperature, aircraft angles of bank, engine performance, and electric load demand are just a few of the metrics to incorporate. That would provide a more holistic model to help engineers identify friction points in design without wasted time often encountered during hardware testing.

APPENDIX

A. CIGS SOLAR CELL SIMULATION

```
% Solar Panel Simulation Model
% (Adapted from [20])

function I = Iphoton(V, G, T)
% I - output current (ampere)
% V - output voltage (volt)
% G - operating solar irradiation (kW m-2)
% T - operating temperature (C)
% k - Boltzmann's constant (J/K or m2 kg s-2 K-1)
% q - electron charge (coulomb)
% n - quality factor dependent of the PV characteristics
% Ns - number of cell in series
% Tr - reference temperature at STC (K)
% Ta - actual temperature of operation (K)
% Voc - open-circuit voltage (volt)
% Isc - short-circuit current (ampere)
% Io - cell leakage current (ampere)
% Iph - photo current (ampere)

% Universal Constants
q = 1.602e-19; % Charge of Electron
k = 1.38e-23; % Boltzman Constant

% Temperature Coefficients (Kelvin = 273.15 + Celcius)
Tr = 273.15 + 25; % Reference temperature - 25 Deg C
Ta = 273.15 + T; % Actual temperature

% Module performance based on cell characteristics from datasheet
% Source: [16].

n = 2; % calculated quality factor
Vtr = (n*k*Tr)/q; % Voltage Coefficient at reference temp
Io = (1.4-0.0003*1.4*(Ta-Tr))...% leakage current adjusted for temp
/(exp(q*(0.667-0.0033*...
0.667*(Ta-Tr))/n/k/Tr)-1);
Isc = 1.4; % Short-circuit Current per cell (STC)
Voc = Vtr*log(Isc/Io+1); % Open-circuit Voltage per cell (STC)

Ns = 36; % Number of cells on surface
Vc = V/Ns; % Per cell voltage of module

Iph = G * Isc; % photo current for irradiance

I = Iph - Io * (exp(Vc/Vtr)-1); % Current generated at each voltage
end
```

B. PERTURB AND OBSERVE ALGORITHM

```
function D = PandO(V_in,I_in, T)
%*****
%MATLAB implementation of Perturb and Observe algorithm
%for MPPT. This algorithm is designed to operate with a
%buck converter (Adapted from [21])
%*****

%Define internal values for the voltage and power as persistent
variables
persistent Dprev Pprev Vprev n

%Initialize the internal values for the voltage and power on first pass
if isempty(Dprev)
Dprev = 0.5;
Vprev = 3;
Pprev = 10;
n = 1;
end

% Initialize algorithm parameters
deltaD = 0.01;

% calculate measured array power

P_in = V_in*I_in;

if (T > n*0.01)
n = n + 1;

% Increase or decrease duty cycle base on conditions
if (abs(P_in-Pprev)) >= 0.1
if (P_in-Pprev) > 0
if (V_in-Vprev) > 0
D = Dprev - deltaD;
else
D = Dprev + deltaD;
end
else
if (V_in-Vprev) > 0
D = Dprev + deltaD;
else
D = Dprev - deltaD;
end
end
else
D = Dprev;
end
Vprev = V_in;
Pprev = P_in;
else
```



```

D = Dprev;
end

% code to avoid duty less than 0.1 and more than 0.9
if (D<0.1)
D=0.1;
elseif (D>0.9)
D=0.9;
end

% Update internal values
Dprev = D;

end

```

C. ENVIRONMENTAL CONDITIONS SIMULATION

```

function [G,T] = Sun(time)

% G = irradiance in kW/m^2
% T = temperature in degrees Celsius
% time = current simulation time used to change environmental
conditions

if isempty(time)
time = 0;
end

time = time / 60;

if (time < 2)
G = 1;
T = 50;
elseif (time < 4)
G = 0.8;
T = 45;
elseif (time < 6)
G = 0.6;
T = 40;
elseif (time < 8)
G = 0.4;
T = 35;
elseif (time < 10)
G = 0.2;
T = 30;
elseif (time < 12)
G = 0.4;
T = 35;
elseif (time < 14)
G = 0.6;
T = 40;
elseif (time < 16)
G = 0.8;

```

```

T = 45;
elseif (time < 18)
G = 1;
T = 50;
elseif (time < 20)
G = 1;
T = 50;
elseif (time < 25)
G = 0.5;
T = 50;
elseif (time < 40)
G = 1;
T = 50;
elseif (time < 43)
G = 1;
T = 50;
elseif (time < 44)
G = 0.9;
T = 50;
elseif (time < 47)
G = 1;
T = 50;
elseif (time < 48)
G = 0.9;
T = 50;
elseif (time < 51)
G = 1;
T = 50;
elseif (time < 52)
G = 0.9;
T = 50;
elseif (time < 55)
G = 1;
T = 50;
elseif (time < 56)
G = 0.9;
T = 50;
elseif (time < 59)
G = 1;
T = 50;
elseif (time < 60)
G = 0.9;
T = 50;
else
G = 1;
T = 50;
end
end

```

LIST OF REFERENCES

- [1] Marine Corps Expeditionary Energy Office. (n.d.). Headquarters Marine Corps. [Online]. Available: <http://www.hqmc.marines.mil/e2o/Mission-Vision/>. Accessed Mar. 28, 2017.
- [2] D. Bathmann. (2010, Aug. 2). Army deploys innovative battery-recharging kit [Online]. Available: <https://www.army.mil/article/43176/army-deploys-innovative-battery-recharging-kit>.
- [3] United States Army Acquisition Support Center. (n.d.). NETT Warrior (NW) [Online]. Available: <http://asc.army.mil/web/portfolio-item/soldier-nw/>. Accessed 28 March 2017.
- [4] C. K. Chin, “Extending the endurance, missions and capabilities of most UAVs, using advanced flexible/ridged solar cells and using new high power density batteries technology,” M.S. thesis, ECE Dept., Naval Postgraduate School, Monterey, CA, 2011. [Online]. Available: <https://calhoun.nps.edu/handle/10945/5824>
- [5] C. Honsberg and S. Bowden. (n.d.). Photovoltaic education (PVCDROM) [Online]. Available: www.pveducation.org. Accessed March 2017.
- [6] S. Michael, “Solar Energy,” class notes for EC3240, Department of Electrical and Computer Engineering, Naval Postgraduate School, Monterey, CA, summer 2016.
- [7] Vishay General Semiconductor, “Solar cell bypass diodes in silicon crystalline photovoltaic panels,” Vishay Intertechnology, Inc., Malvern, PA, 2011.
- [8] S. Bush. (2011, Sept. 22). “Lossless” power diode drops only 50mV. *Electronics Weekly*. [Online]. Available: <http://www.electronicsexpress.com/market-sectors/power/lossless-power-diode-drops-only-50mv-2011-09/>
- [9] N. Femia, et al., *Power Electronics and Control Techniques for Maximum Energy Harvesting in Photovoltaic Systems*, 1st ed., New York, NY: CRC Press, 2014, pp. 1–308.
- [10] G. Petrone, G. Spagnuolo, and M. Vitelli, “TEODI: A new technique for Distributed Maximum Power Point Tracking PV Applications,” in *International Conference on Industrial Technology*, Vina del Mar, Chile, 2010, pp. 982–987.
- [11] C. Stephenson, “Utilizing maximum power point trackers in parallel to maximize the power output of a solar (photovoltaic) array,” M.S. thesis, ECE Dept., Naval Postgraduate School, Monterey, CA, 2005.

- [12] B. Buckley. (n.d.). Maximum power point tracking [Online]. Available: <http://bryanwbuckley.com/projects/mppt.html>. Accessed 24 March 2017.
- [13] Ant. (n.d.). C2000 solar MPPT tutorial Pt/3 [Online]. Available: <http://codertronics.com/c2000-solar-mppt-tutorial-pt3/>. Accessed 24 March 2017.
- [14] N. Mohan, et al., “DC-DC switch-mode converters,” in *Power Electronics: Converters, Applications, and Design*, 3 ed., Hoboken, NJ: John Wiley & Sons, 2003, ch. 7, pp. 161–184.
- [15] R. Ashton, “Popular Direct-Coupled DC-DC Converters,” class notes for EC3150, Department of Electrical and Computer Engineering, Naval Postgraduate School, Monterey, CA, summer 2016.
- [16] Global Solar Energy, Inc., “Product datasheet: FG-SM12-11: 8.3W (6V) Solar submodule,” Global Solar Energy, Inc., Tucson, AZ, 2016.
- [17] *Small Unmanned Aircraft System (SUAS) Puma AE II with Digital Data Link Operator’s Manual*, AeroVironment, Inc., Monrovia, CA, 2015.
- [18] M. Billings, “Application of interdigitated back contact silicon photovoltaic cells to extend the endurance of small unmanned aerial systems,” M.S. thesis, ECE Dept., Naval Postgraduate School, Monterey, CA, 2016.
- [19] R. Parenti, “Fly forever: Using high efficiency and lightweight GaAs solar as an auxiliary UAV,” conference notes for presentation at Cruiser TechCon, Naval Postgraduate School, Monterey, CA, 2017.
- [20] S. Lodwal, *Solar MPPT with Resistive Load*, New Dehli, India: Dehli Technological University, 2014.
- [21] C. Osario, *Modeling and Simulation of PV Power Converters*, Natick, MA: Mathworks, 2011.

INITIAL DISTRIBUTION LIST

1. Defense Technical Information Center
Ft. Belvoir, Virginia
2. Dudley Knox Library
Naval Postgraduate School
Monterey, California